Supporting Information

Selective electrochemical nitrogen fixation to ammonia catalyzed by a novel microporous vanadium phosphonate via the distal pathway

Smruti Vardhan Purohit,[ab] ‡ Rupali Ipsita Mohanty,[ab] ‡ Bibek Dash,[a] Piyali Bhanja*[a] and Bikash Kumar Jena *[ab]

[a]*CSIR-Institute of Minerals and Materials Technology, Bhubaneswar-751013, India*

[b]*Academy of Scientific and Innovative Research (AcSIR), Ghaziabad-201002, India*

‡ *S.V. Purohit and R. I. Mohanty contributed equally to this work.*

Corresponding author: piyalibhanja4@gmail.com, bikash@immt.res.in

Title of the section	Page number
Experimental Section	**S5**
Synthesis method of microporous vanadium phosphonate (VPn)	**S5**
Electrochemical Measurements	**S6**
Computational Details	**S7**
Instrumentation	**S7**
Preparation of working electrode	**S8**
Detection of NO_x impurities in Ar, $^{14}N_2$, and $^{15}N_2$ gas supplies	**S9**
Determination of produced ammonia	**S9**
Determination of hydrazine	**S11**
Calculation of FE and yield rate of NH_3	**S11**
$^{15}N_2$ isotope labeling experiment	**S12**
The schematic representation of the synthesis route of VPn.	**S12**
Table S1: Indexing table for VPn.	**S13**
Figure S1: EDS and elemental mapping analysis with corresponding TEM images of as-synthesized VPn material.	**S14**
Figure S2: FTIR spectrum of VPn material.	**S15**
Figure S3: Raman spectrum of VPn material.	**S16**
Figure S4: Narrow range XPS spectrum of VPn containing elements V 2p, P 2p, O 1s, C 1s.	**S17**
Figure S5. Photograph of the experimental setup and electrochemical cell	**S18**
Figure S6: UV-visible absorbance curves for standard nitrite, nitrate, and ammonia solutions with different concentrations and respective calibration curves obtained from the same.	**S19**
Figure S7: UV-visible absorbance curves for gas supplies (Ar, $^{14}N_2$, and $^{15}N_2$) obtained before and after passing through alkaline $KMnO_4$ solution to trap NO_x impurities and acid trap to test NH_4^+ impurities, respectively.	**S20**
Table S2: Summary of the gas impurity analysis by UV-visible spectroscopy (Quantified amounts of NO_x/NH_4^+ impurities before and after purification by scrubbing solution).	**S21**
Figure S8: UV-visible spectrum of the known standard solution of NH_4Cl, Calibration plot for NH_3 detection, and Photograph of standard solutions of NH_4Cl stained with Phenate method indicator after incubation in the dark for 2 h.	**S22**
Figure S9: UV-visible spectrum of the known standard solution of NH_4Cl, Calibration plot for NH_3 detection, and Photograph of standard solutions of NH_4Cl stained with indophenol blue indicator after incubation in the dark for 2 h.	**S23**
Figure S10: UV-visible spectrum of known standard solution of Hydrazine monohydrate, Calibration plot for N_2H_4 detection, and Photograph of standard solutions of Hydrazine monohydrate stained with indicator after incubation in the dark for 30 min.	**S24**
Figure S11: UV-visible spectra of the stained electrolytes after 2 h electrolysis at different potentials by phenate and indophenol blue methods, respectively.	**S25**
Figure S12: UV-visible spectra of resultant electrolytes after 2 h of electrolysis at different potentials stained with the indicator for hydrazine detection and Photograph of corresponding electrolytes stained with indicator after incubation in the dark for 30 min.	**S26**

Figure S13: UV-visible spectra of the electrolyte after different control experiments (at open circuit potential (OCP), with Ar feed gas at -0.6 V for 7200 s on the VPn loaded CP (VPn/CP@-0.6V, Ar), with N_2 feed gas at -0.6 V for 7200 s on the bare Carbon paper (CP), and at -0.6 V with VPn modified CP in N_2 saturated electrolyte (VPn/CP@-0.6V, N_2) and Yield rate of NH_3 at four different control experiments.	**S27**
Figure S14: Chronoamperometry (i-t) curve of five consecutive cyclic tests of VPn at -0.6 V, UV-visible spectra of the stained electrolytes after 2 h electrolysis during five consecutive cyclic tests at -0.6 V by phenate method and indophenol blue method respectively, Yield rate of NH_3 and faradaic efficiency (FE) calculated for five consecutive cyclic tests of VPn at -0.6 V..	**S28**
Figure S15: Long-term stability test of VPn over 15 h of electrochemical NRR.	**S29**
Figure S16: ^{1}H NMR qualitative and quantitative analysis after isotopic labeling experiments employed on VPn catalyst in the $^{15}N_2$ and $^{14}N_2$ as the feed gas.	**S30**
Figure S17: CV curves in the non-Faradaic region at various scan rates (10 to 200 mV s^{-1}) for VPn material in 0.1M Na_2SO_4 and the corresponding fitted plot of scan rate vs. the anodic and cathodic current difference.	**S31**
Figure S18: Nyquist plot for the electrochemical impedance measurements of the VPn material in N_2 and Ar saturated electrolyte at -0.6 V vs. RHE with a fitted equivalent circuit in the inset.	**S32**
Figure S19: Zeta potential distribution curve for VPn material.	**S33**
Figure S20: Surface contact angle measurement of VPn material.	**S34**
Figure S21: FE-SEM images of VPn at different scales after durability test.	**S35**
Figure S22: TEM images of VPn catalyst after durability test.	**S36**
Figure S23: EDS and elemental mapping with corresponding TEM images of VPn catalyst after durability test.	**S37**
Figure S24: Wide angle powder XRD pattern of the as-prepared VPn material after a long cycling test.	**S38**
Figure S25: Raman spectrum of the as-prepared VPn material after a long cycling test.	**S39**
Figure S26: Narrow range XPS spectrum of VPn containing elements V 2p, P 2p, O 1s, C 1s, after long cycling test.	**S40**
Figure S27: DFT optimised structure of as-synthesized VPn.	**S41**
Figure S28: Optimized DFT structures of the as-prepared VPn material and all the intermediates involved in the NRR mechanism.	**S42**
Table S3. Optimized coordinates of VPn material.	**S43**
Table S4. Optimized coordinates of *N_2	**S44**
Table S5. Optimized coordinates of *NNH	**S45**
Table S6. Optimized coordinates of *NHNH	**S46**
Table S7. Optimized coordinates of *$NHNH_2$	**S47**
Table S8. Optimized coordinates of *NH_2NH_2	**S48**
Table S9. Optimized coordinates of *NNH_2	**S49**
Table S10. Optimized coordinates of *N	**S50**
Table S11. Optimized coordinates of *NH	**S51**
Table S12. Optimized coordinates of *NH_2	**S52**
Table S13. Optimized coordinates of *NH_3	**S53**
Figure S29: Schematic diagram showing the two possible pathways (associative alternating and associative distal) involving all the DFT optimized structures for the electrochemical NRR over VPn catalyst.	**S54**

Figure S30: Projected density of states (PDOS) of N_2 and V 3d orbitals before and after N_2 adsorption near the Fermi level when the Fermi level is set to zero.	**S55**
Importance and performance of the vanadium phosphonate with respect to the vanadium oxides, phosphides, and sulfides.	**S56**
Table S14: Performance of other vanadium-based electrocatalysts as compared to VPn.	**S58**
Table S15: Comparison table with recently reported NRR electrocatalyst.	**S59**
References	**S61**

Experimental Section

Chemicals: Phenylphosphinic acid (M = 142.09 g/mol) and vanadium (III) chloride (M = 157.30 g/mol) were purchased from Sigma Aldrich India. Aqueous ammonium hydroxide (25 wt%) solution was received from Merck to maintain the pH of the reaction mixture. Sodium sulfate was purchased from Alfa-Aesar, Phenol, 4-Dimethylaminobenzaldehyde, and Hydrazine monohydrate was obtained from TCI. Sodium nitroferricyanide (III) dihydrate, Trisodium citrate, Salicylic acid, sulphanilamide, N-(1-napthyl) ethylenediamine dihydrochloride and Sodium hypochlorite solution were received from Sigma-Aldrich, India. Sodium hydroxide, HCl, Potassium nitrate, Sodium nitrite, and Ammonium chloride were purchased from HIMEDIA. Other organic solvents were used as received. Nafion-117 membrane, Nafion solution, Dimethyl sulfoxide-D6, Deuterium oxide, and $^{15}NH_4Cl$ were purchased from Sigma-Aldrich, India. N_2 (99.999%) and Ar (99.999%) gases are obtained from Biosciences. Other organic solvents were also obtained from Merck and used for washing without any purification. Purchased Chemicals were used without further purification. Deionized water was used throughout the experiment.

Synthesis method of microporous Vanadium phosphonate:

To synthesize the microporous vanadium phosphonate, 1 mmol (142 mg) of phenylphosphinic acid, an organophosphorus ligand, was dissolved in 7 mL of distilled water. After 5 minutes of continuous stirring, an aqueous solution of 2 mmol (314 mg) vanadium (III) chloride was mixed with the transparent acidic solution mixture and allowed to stir vigorously for 30 minutes. Then, an aqueous ammonia solution was added dropwise during continuous stirring to maintain the pH of the reaction mixture to 6.5. The final homogeneous gel was obtained after 2 h of vigorous stirring and poured into the Teflon-lined stainless-steel autoclave at 160 °C for 48 hours. After completion, the solid dark green coloured product was collected through

the centrifugation technique and washed properly with distilled water, followed by ethanol to remove unreacted substances from the material surface. The product was dried overnight in a vacuum oven at 70 °C and named as VPn. The collected sample has been subjected to thorough characterization and electrochemical measurements. **Scheme S1** represents the outline for vanadium phosphonate (VPn) synthesis under hydrothermal reaction conditions.

Electrochemical Measurements:

The electrochemical NRR measurements were carried out at room temperature on a CHI-760D workstation (CH-Instrument) in a standard three-electrode system using modified carbon paper as the working electrode, graphite rod as the counter electrode and Ag/AgCl electrode as the reference electrode. An H-shaped electrochemical cell was used for all the electrochemical experiments. The Nafion-117 membrane was introduced between the two compartments as a separator, and 40 ml of 0.1M Na_2SO_4 was taken as a working electrolyte in each chamber. Before electrochemical testing, the Nafion-117 membrane was pre-treated by heating successively in 5% H_2O_2 solution, 0.5 M H_2SO_4, and ultrapure water at 80 °C for 1.5 h. Purified N_2(99.999%) and Ar(99.999%) feed gases were used during the experiments, and the purification was done using an alkaline $KMnO_4$ trap and dilute acid traps to remove any impurities and contamination as per the reported protocol.[1-3] Before any electrochemical experiment, purified Ar/N_2 gas was passed through the cathodic chamber for at least 30 minutes and then was continuously bubbled at a constant rate throughout the chronoamperometric experiments. The potentials reported in this work were converted to the RHE scale via calibration with the following equation: E (vs. RHE) =E (vs Ag/AgCl) + 0.197 + 0.059 × pH. The LSV curves were obtained at a scan rate of 5 mVs^{-1} with IR compensation at room temperature. The Chronoamperometry tests at different applied voltages were performed with continuous magnetic bead stirring at 350 rpm for 2 h to reduce nitrogen under ambient conditions. Cyclic Voltammetry (CV) has been taken at various scan rates (10, 20, 40, 60, 80,

100, 150, and 200 mV/s) in the non-faradic potential range of 0.74-0.84 V vs. RHE and is used to estimate the double-layer capacitance (Cdl). The electrochemical impedance spectroscopy (EIS) measurement of the phosphonate sample was performed in the frequency range of 10^{-5} to 0.1 Hz in the Ar and N_2-saturated 0.1 M Na_2SO_4 solution at -0.6 V vs. RHE.

Computational Details:

DFT calculations were performed using the linear combination of atomic orbitals (LCAO) method as implemented in the Quantum ATK (Synopsys, USA) package.[4] The exchange-correlation of electrons was included using the Generalized Gradient Approximation (GGA) of the Perdew-Burke-Ernzerhof (PBE) correlation function.[5] The van der Waals interactions were taken care of using DFT-D2 of Grimme's method.[6] Brillouin zone is sampled using a Monkhorst-Pack mesh of 9x9x9 k-points for all the geometry optimization and electronic structure calculations.[7] The convergence criteria of 10^{-5} eV and 10^{-2} eV Å $^{-1}$ are used for the energy and forces until all geometrical structures are relaxed.

The Gibbs free energy change (ΔG) in each hydrogenation step involved in the electrochemical NRR process was obtained by following the computational hydrogen electrode (CHE) model proposed by Nørskov et al.[8] Based on the above model, ΔG values can be calculated by the following equation [Eq. (1)]; $\Delta G = \Delta E + \Delta ZPE - T\Delta S$ **(1)**

Where ΔE is the adsorption energy calculated by DFT, ΔZPE, and TΔS are the changes in the zero-point energies and the entropy, respectively, at the room temperature (T = 298.15 K).

ΔE can be calculated by the following equation [Eq. (2)]; $\Delta E = E^*_{ads} - E_{ads} - E^*$ **(2)**

E^*_{ads}, E_{ads}, and E* are the total energies for adsorbed species on the catalyst, adsorbed species, and isolated catalyst. The experimental data at 298.15 K were taken from the NIST database for the gaseous molecules.

Instrumentation:

Rigaku RINT 2500X diffractometer with monochromated Cu Kα radiation (40 kV, 40 mA) at a scan rate of 0.1° min^{-1} has been utilized to analyze the wide-angle powder X-ray diffraction (XRD) pattern for the as-synthesized materials. Unit cell parameters of the vanadium phosphonate were obtained from the EXPO 2014 software with the built-in Rietveld refinement of the experimental powder XRD data.[9] The FT-IR spectrum of the VPn was recorded using Thermo Scientific Nicolet 4700 spectrometer, where the KBr pellet was used as a background reference. The nitrogen sorption isotherm and the pore size diameter of the as-prepared sample were measured by the Quantachrome Autosorb after degassing the sample at 150 °C for 8 h. The scanning electron microscope (SEM) images of the material were observed from Hitachi SU-8000 SEM, where the accelerating voltage was 15 kV. The TEM images and elemental mapping for all samples were taken by an FEI F20 FEG-STEM instrument after drop-casting the sample onto the copper grid. To analyze the oxidation states of the metal centre of as-prepared three metal phosphonate materials, the X-ray photoelectron spectroscopy technique was used with Kratos Axis Ultra XPS. A UV-visible spectrophotometer (UV-2600, Shimadzu) was utilized to record the UV-visible spectra. Contact angle measurement was recorded using a Phoenix multi-water contact instrument. Zeta potential measurement was done using the Litesizer 500 (Anton Paar) instrument. ^{1}H NMR spectra were recorded on a Jeol NMR spectrometer (400 MHz) for the isotope labeling experiment. The Raman spectrum of the VPn was recorded using a Renishaw microscopic confocal Raman spectrometer with a laser wavelength of 532 nm.

Preparation of working electrode:

To prepare the working electrode, 1 mg of the as-prepared material was suspended in 195 µL of ethanol and 5 µL of 5% Nafion solution. The resulting suspension was sonicated for 1 hour to get a homogeneous ink. Then 100 µL of the so prepared ink was drop-casted onto a carbon paper (1 cm ×1 cm) and was dried under ambient conditions.

Detection of NO_x impurities in Ar, $^{14}N_2$, and $^{15}N_2$ gas supplies:

Griess spectrophotometric assay was applied to quantify the amount of NO_x contaminants.[1-3] Griess reagents and reducing agent solution were freshly prepared and stored in the refrigerator (ca 4 °C) in the dark. The life cycle of the testing kit was estimated to be not more than 4 weeks for reliable results. Diazotising reagent was obtained by adding 0.1 g sulphanilamide (SULF) and 1 mL concentrated HCl to the total volume of 10 mL with water in a volumetric flask. A coupling reagent was prepared by dissolving 0.01 g of N-(1-napthyl) ethylenediamine dihydrochloride (NED) in 10 mL water. In a volumetric flask, the reducing agent solution was dissolved by 0.5 g VCl_3 in 25 mL of 6 M HCl(aq.). After adding VCl_3, the mixture was kept in the dark for 1 h before being filtered and transferred into an amber bottle.

In the standard testing protocol, 1000 μL of the sample was taken, and 50 μL of pre-mixed solution of SULF and NED (1:1 vol.) was added to it. After that, the obtained mixture was incubated under ambient conditions for 20 min. Then, the UV–vis spectrum in a 400–800 nm range was recorded to detect NO_2^-. For nitrate analysis, 50 μL of reducing agent solution was added to the above mixture and kept at 60 °C (water bath) for 25 min. Finally, the solution was cooled down to room temperature and analyzed by UV–vis again within the same wavelength range. The concentrations of nitrite and nitrate as a function of the absorbance value at the wavelength of 540 nm were calculated by using calibration plots constructed with standard $NaNO_2$ and KNO_3 solutions.

Determination of produced ammonia (NH_3):

Phenate Method:

Stock Reagents:

1. Phenol solution: 5 g phenol was dissolved in 50 mL 95% ethanol;

2. Sodium nitroferricyanide solution: 0.25 g Sodium nitroferricyanide (III) dihydrate was dissolved in 50 mL Millipore water;
3. Alkaline complexing reagent: 20 g trisodium citrate and 1 g sodium hydroxide were dissolved in 100 mL Millipore water;
4. Sodium hypochlorite solution
5. Oxidizing solution: 6 mL alkaline solution (3) was added to 1.5 mL sodium hypochlorite solution (4).

The concentration of ammonia produced in the electrolyte after the 2-hour electrolysis was measured using the phenate method. In detail, 5 mL of the electrolyte after N_2 reduction for 2 hours was added into 0.2 mL of phenol solution (1), then added 0.2 mL of Sodium nitroferricyanide solution (2), and finally added to 0.5 mL of oxidizing solution (5). The Ultraviolet-Visible absorption spectra were recorded after the above mixture was stored in darkness for 2 hours, which exhibited an absorption peak at 640 nm for the blue-colored solutions.

For the concentration-absorbance calibration curve, the standard ammonium chloride solution (0.1 M Na_2SO_4 as mother solution) with a series of concentrations (0, 0.1, 0.2, 0.4, 0.6, 0.8, and 1 μg. mL^{-1}) were prepared, and the concentration was determined by the phenate method using the absorbance at a wavelength of 640 nm. The fitting curve ($y = 0.97592x + 0.01052$, $R^2 = 0.999$) shows a good linear relation of absorbance value with NH_4Cl concentration.

Indophenol Blue Method:

The concentration of the ammonia produced via the electrocatalytic NRR was determined using the indophenol blue method. In detail, 2 mL of the post-NRR electrolyte was removed from the cathodic chamber and added into 2 mL NaOH solution (1 M) containing 5 wt% salicylic acid and 5 wt% sodium citrate, then followed by the addition of 1 mL NaClO (0.05 M) and 0.2 mL $C_5FeN_6Na_2O$ (sodium nitroferricyanide) aqueous solution (1wt%). After standing in

darkness for 2 hours, the absorption spectrum was measured using a UV-vis spectrophotometer. The formation of indophenol blue was determined using the absorbance at a wavelength of 655 nm.

For the concentration-absorbance calibration curve, the standard ammonium chloride solution (0.1 M Na_2SO_4 as mother solution) with a series of concentrations (0, 0.1, 0.2, 0.4, 0.6, 0.8, and 1 μg.mL^{-1}) were prepared. The concentration was determined by the above indophenol method using the absorbance at a wavelength of 655 nm. The fitting curve ($y = 0.39183x + 0.03276$, $R^2 = 0.999$) shows a good linear relation of absorbance value with NH_4Cl concentration. Also, for the adventitious ammonia impurity analysis, the standardisation and the quantification of contamination in the gas supplies were done using this method.

Determination of hydrazine (N_2H_4) by Watt−Chrisp method:

The concentration of hydrazine in the electrolyte after the 2-hour electrolysis was determined by the Watt and Chrisp method. In detail, a mixture of ethanol (30mL), HCl (concentrated, 3 mL), and 4-dimethylaminobenzaldehyde (0.599 g) was prepared as a colour reagent. 2 ml of the above colour reagent was added to 2 mL of the electrolyte after 2-hour electrolysis. The Ultraviolet-Visible absorption spectra were recorded after the above mixture was stored in darkness for 30 minutes, which exhibited an absorption peak at 455 nm.

For the concentration-absorbance calibration curve, the standard hydrazine monohydrate solution (0.1 M Na_2SO_4 as mother solution) with a series of concentrations (0, 0.1, 0.2, 0.4, 0.6, 0.8, and 1 μg.ml^{-1}) were prepared. The concentration was determined by the Watt and Chrisp method using the absorbance at a wavelength of 455 nm. The fitting curve ($y = 0.52645x + 0.00514$, $R^2 = 0.996$) shows a good linear relation of absorbance value with N_2H_4 concentration.

Calculation of FE and yield rate of NH_3 :

NH_3 yield rate can be calculated as follows:

$$V_{NH3}(\mu g\ h^{-1}\ m_{cat}^{-1}) = \frac{C_{NH3} \times V_{electrolyte}}{t \times m_{cat}}$$

Faradic efficiency can be calculated as follows:

$$FE\ (\%) = \frac{3\times F \times C_{NH3} \times V_{electrolyte}}{17 \times Q} \times 100$$

Where, constant 3 is the transfer electron number of produced NH_3, C_{NH3} (μg mL^{-1}) is the concentration of produced NH_3, $V_{electrolyte}$ (40 mL in our work) is the volume of the electrolyte, F (96485 C mol^{-1}) is the Faraday constant, constant 17 is the molar mass of NH_3, Q (C) amount of electricity consumed in the electrolysis process, t (=2 h) is the time for electrolysis and m_{cat} is the loading mass of electrocatalyst (0.5 mg).

$^{15}N_2$ isotope labeling experiment:

$^{15}N_2$ (98 atom % ^{15}N, purchased from Sigma-Aldrich) served as feeding gas for the isotopic labeling experiment. The gas purification (with alkaline $KMnO_4$ trap and dilute acid traps) and electrochemical experiments were the same as the measurements in $^{14}N_2$. The chronoamperometry tests were performed at -0.6 V vs. RHE in 0.1 M Na_2SO_4. To prepare the NMR sample, 10 μL of 0.5 M H_2SO_4 was added into 600 μL electrolyte, followed by 70 μL D_2O and 30 μL dimethyl sulfoxide.[10] The above solution was subjected to ^1H nuclear magnetic resonance analysis. The calibration curves were obtained from ^1H NMR spectrum of standard $^{14}NH_4Cl$ and $^{15}NH_4Cl$ solutions of different concentrations (0 -2.5 μg mL^{-1}).

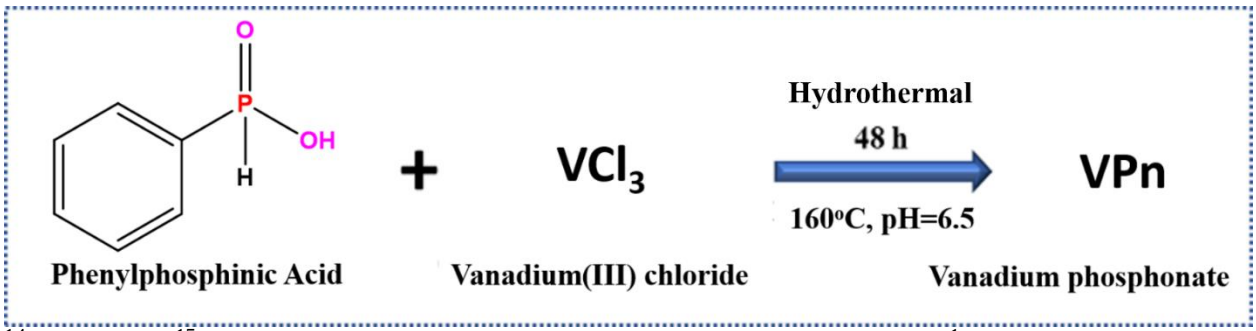

Scheme S1. The schematic representation of the synthesis route of VPn.

Table S1: Indexing table for VPn:

Cell parameters

a = 15.37346 b = 12.47406 c = 9.89154

α = 90.000 β = 93.587 γ = 90.000

Cell volume: 1893.18 Å^3, crystal unit cell structure: tetrahedral

h	***k***	***l***	***2θ***	***d***
1	0	0	5.75525	15.34334
0	0	1	8.95016	9.87216
2	0	0	11.52507	7.67167
1	2	-1	17.58709	5.03864
1	2	1	17.95518	4.93617
0	0	2	17.95551	4.93608
2	2	0	18.31699	4.83947
1	1	2	20.50061	4.32866
2	2	1	20.74024	4.27919
3	1	1	21.26852	4.17407
1	2	-2	23.40625	3.79746
3	2	1	24.63085	3.61136
2	3	-1	25.71204	3.46190
3	0	2	25.83565	3.44562
4	1	1	26.41110	3.37184
3	2	2	29.59445	3.01599
0	2	3	30.69337	2.91046
2	3	2	30.84298	2.89669
3	3	-2	32.52293	2.75079
1	5	0	36.45702	2.46247
6	0	2	40.70587	2.21471
5	4	0	41.23927	2.18729
3	4	3	44.42178	2.03769
7	0	-4	54.15154	1.69230
2	0	6	58.01224	1.58852

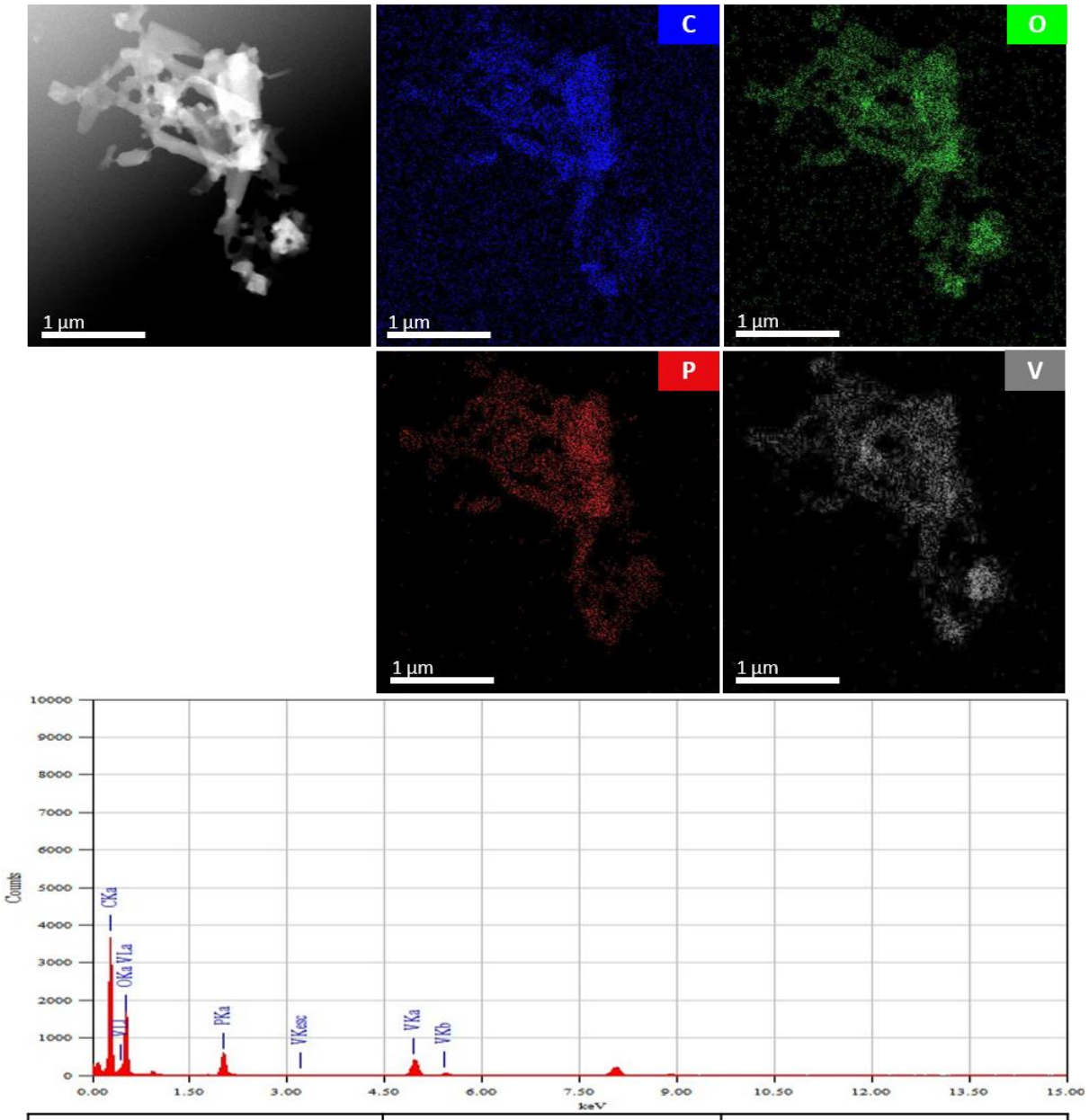

Elements	Mass %	Atom %
C	71.64	82.04
O	15.83	13.61
P	5.56	2.47
V	6.97	1.88

4	3	-6	64.15690	1.45040

Figure S1. EDS and elemental mapping analysis with corresponding TEM images of as-synthesized VPn material.

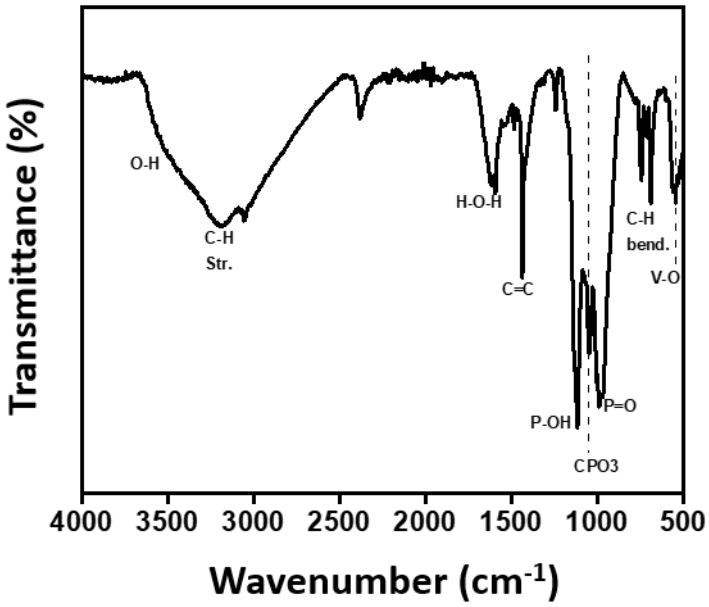

Figure S2. FTIR spectrum of VPn material.

The characteristic signals corresponding to -OH groups, the ring containing C-H groups, water molecules containing H-O-H groups, and C=C groups can be found. The three characteristic peaks at 1124, 1055, and 972 cm^{-1} can be attributed to the phosphonate group containing P-OH, CPO_3, and P=O groups, respectively. Also, the sharp signals observed at 698 cm^{-1} and 558 cm^{-1} are ascribed repetitively as the C-H bending vibration and stretching vibration of V-O bonds.[11,12]

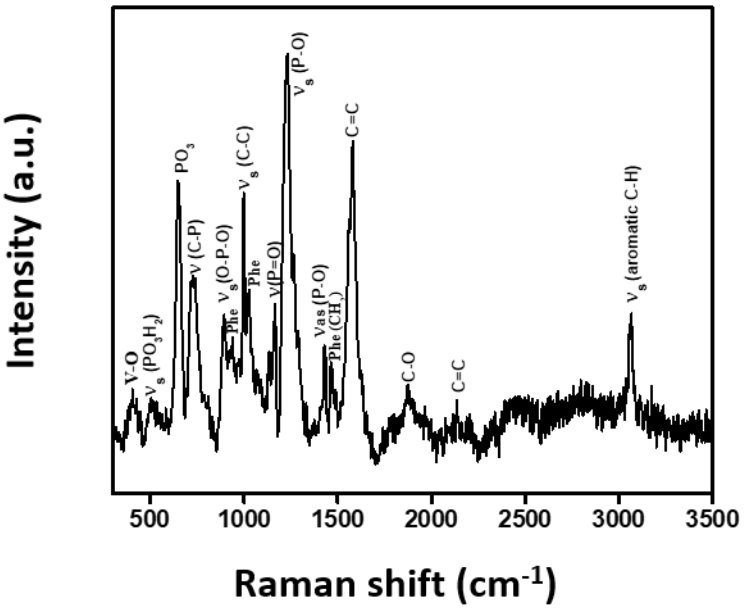

Figure S3. Raman spectrum of VPn material.

The peak at 3070 cm^{-1}, 1228.6 $cm^{-1,}$ and 653 cm^{-1} is due to the aromatic C-H group's symmetric stretching vibration (υ_s), the υ_s(P-O) bond and the presence of a connected PO_3 group respectively. The respective asymmetric stretching vibration (υ_{as}) of the P-O bond was observed at 1284 and 1427 cm^{-1}. Also, the peak at 408 cm^{-1} arises due to the υ_s (PO_3H_2) group, signifying the presence of the aphosphonate group in the matrix. The Raman band at 404.5 cm^{-1} can be attributed to the metal-oxygen bond, bands at 936.3 cm^{-1} and 1030 cm^{-1} correspond to different vibration modes of the phenyl group. The bands at 1165.8 cm^{-1}, 1468.5 cm^{-1} and 1871.7 cm^{-1} corresponds to vibration modes of P=O, phenyl (CH_2) and C-O group respectively. Other peaks at 997 cm^{-1} and 1030 cm^{-1} indicate the vibrational modes for the phenyl ring present in the organophosphorus ligand.[13]

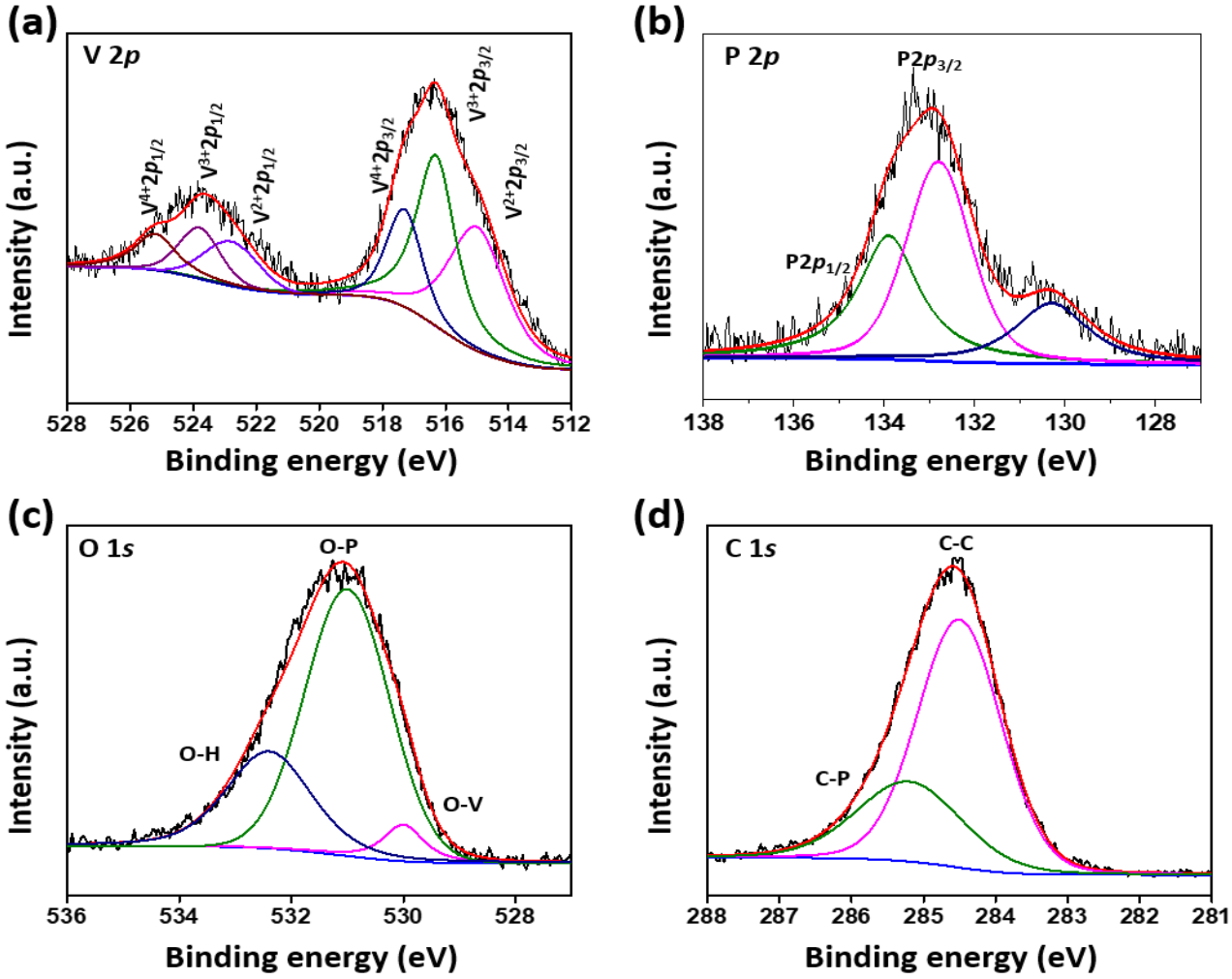

Figure S4. Narrow range XPS spectrum of VPn containing elements (a) V 2p, (b) P 2p, (c) O 1s, (d) C 1s.

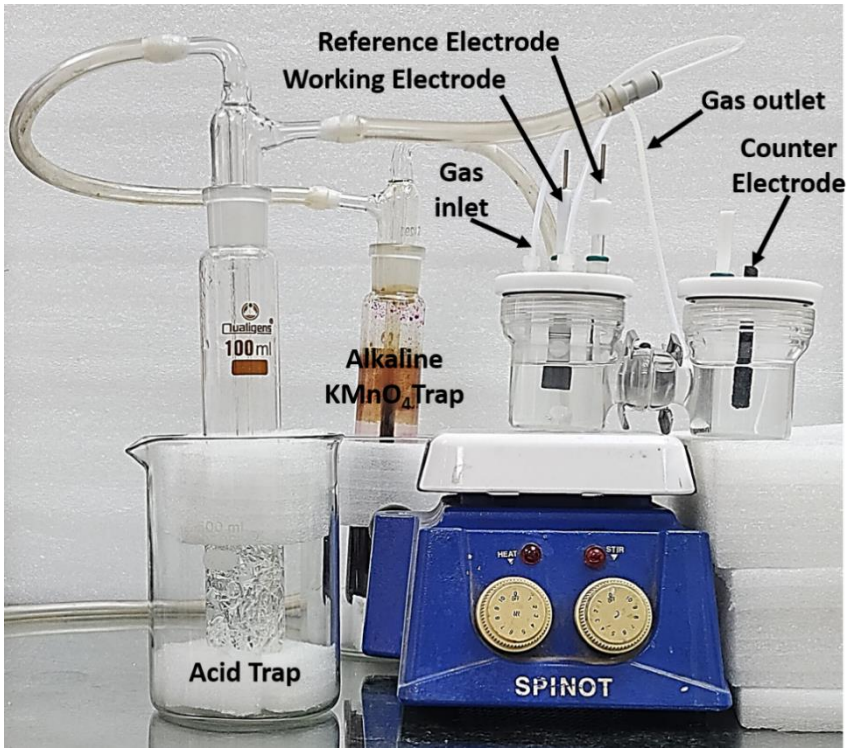

Figure S5. Photograph of the experimental setup and electrochemical cell.

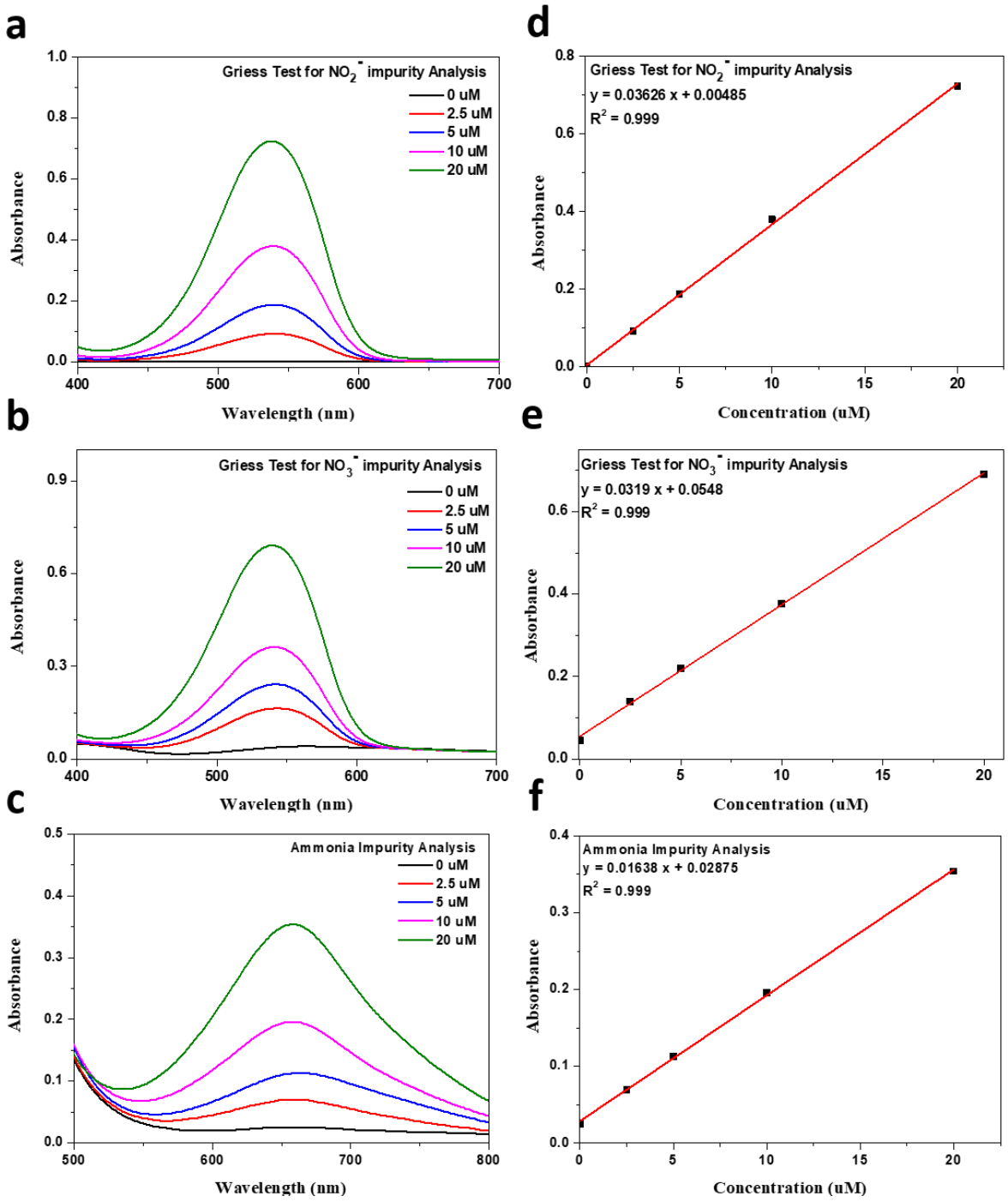

Figure S6. UV-visible absorbance curves for standard (a) nitrite, (b) nitrate, and (c) ammonia solutions with different concentrations and (d-f) respective calibration curves obtained from the same.

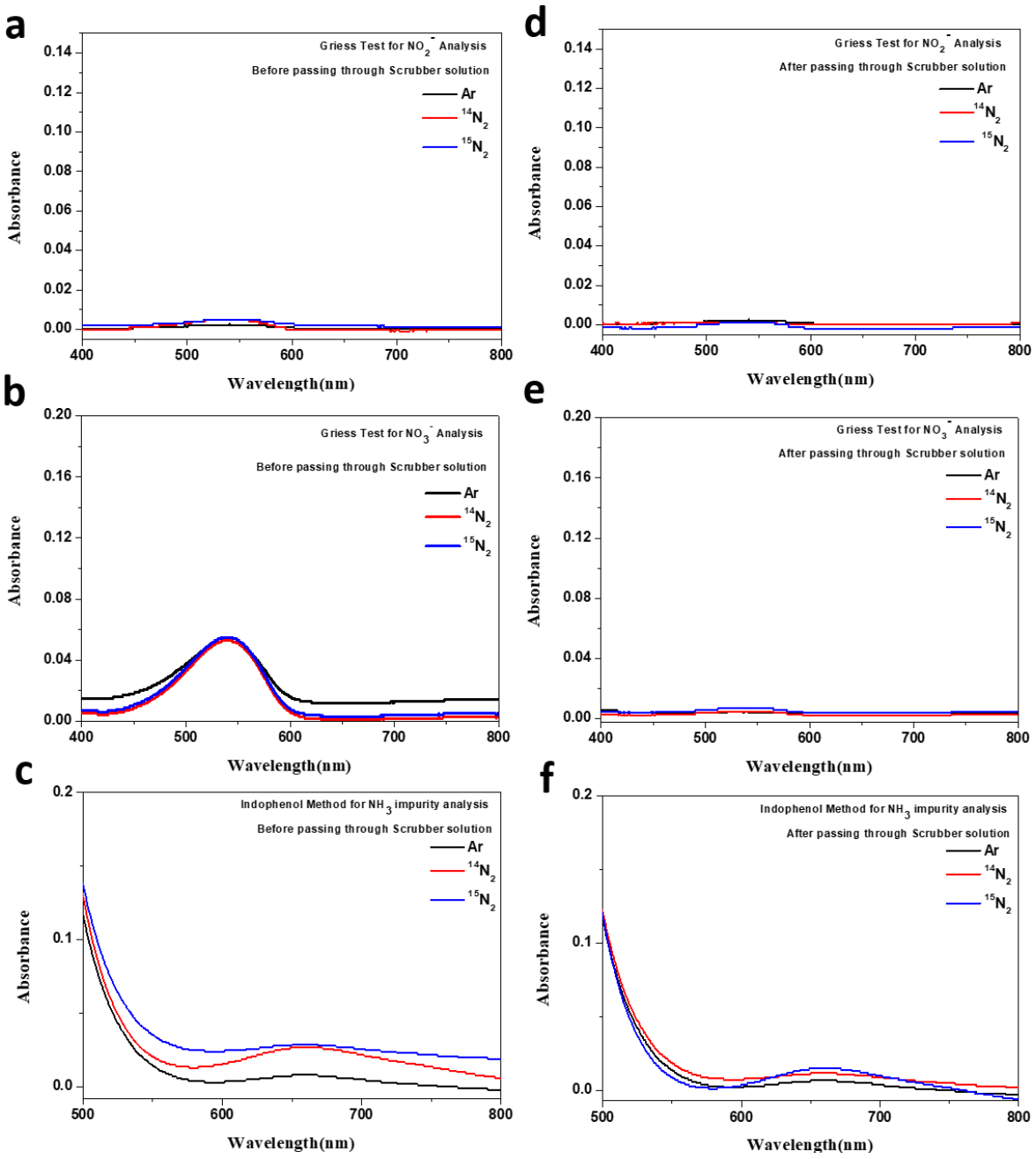

Figure S7. UV-visible absorbance curves for gas supplies (Ar, $^{14}N_2$, and $^{15}N_2$) obtained (a-c) before and (d-f) after passing through alkaline $KMnO_4$ solution to trap NO_x impurities and acid trap to test NH_4^+ impurities, respectively.

Gas Supplies	Before Purification			After Purification		
	NO_2^- (μM)	NO_3^- (μM)	NH_4^+ (μM)	NO_2^- (μM)	NO_3^- (μM)	NH_4^+ (μM)
Ar	-	**0.002**	-	-	**<0.001**	-
$^{14}N_2$	**0.002**	**0.003**	**0.006**	**<0.001**	**<0.001**	**<0.001**
$^{15}N_2$	**0.002**	**0.004**	**0.007**	**<0.001**	**<0.001**	**<0.001**

Table S2. Summary of the gas impurity analysis by UV-visible spectroscopy (Quantified amounts of NO_x/NH_4^+ impurities before and after purification by scrubbing solution).

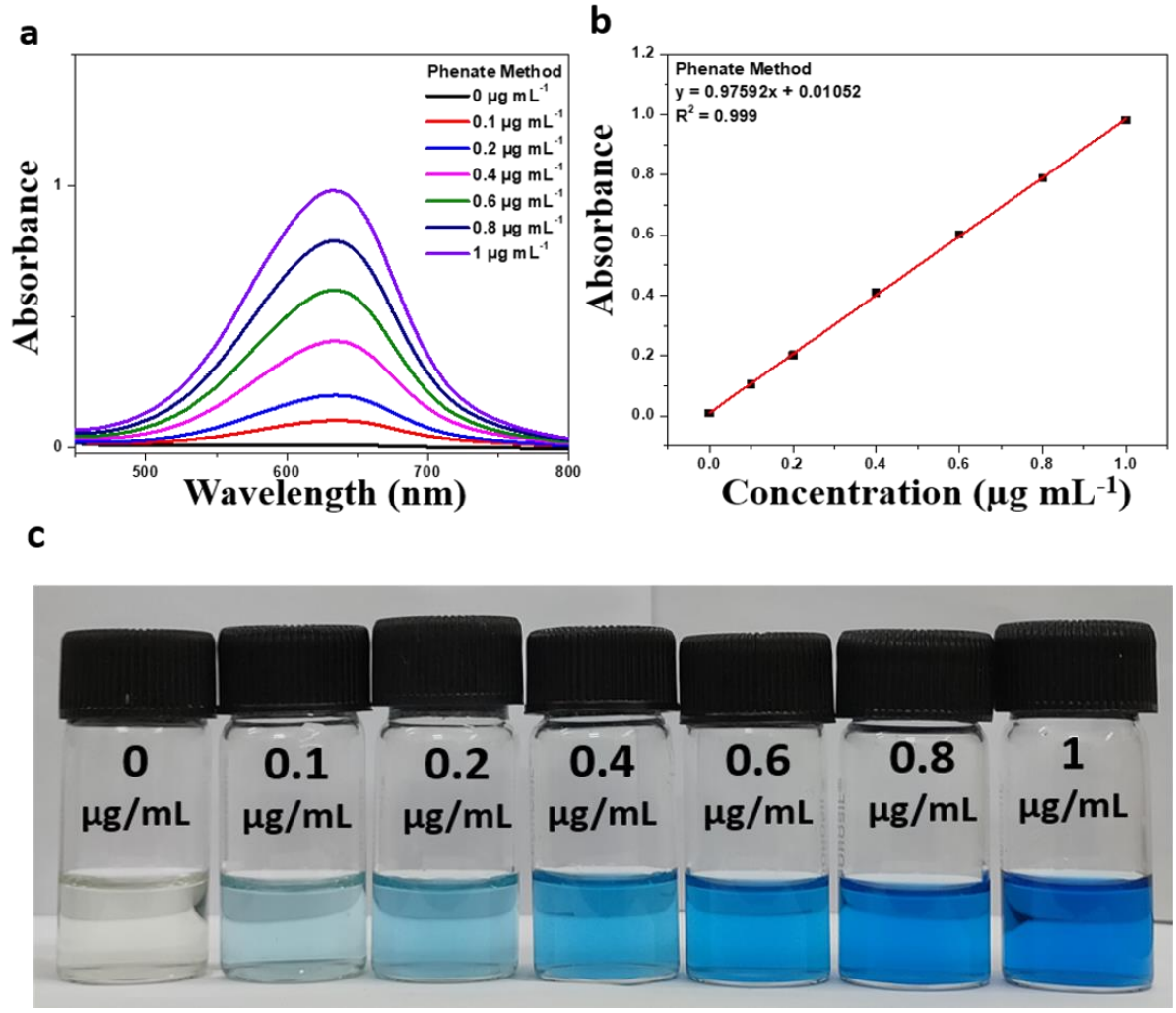

Figure S8. (a) UV-visible spectrum of the known standard solution of NH_4Cl, (b) Calibration plot for NH_3 detection, (c) Photograph of standard solutions of NH_4Cl stained with Phenate method indicator after incubation in the dark for 2 h.

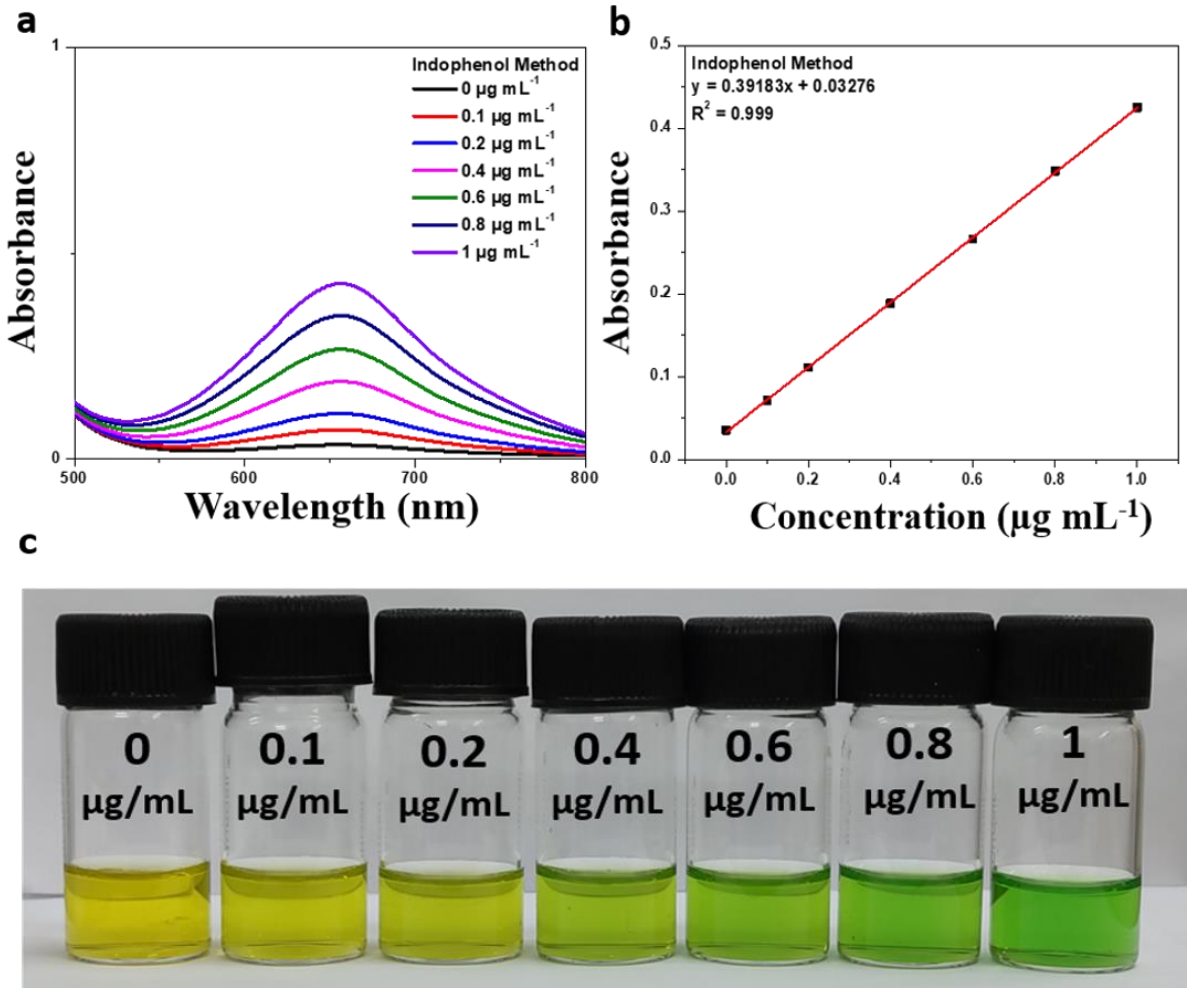

Figure S9. (a) UV-visible spectrum of the known standard solution of NH_4Cl, (b) Calibration plot for NH_3 detection, (c) Photograph of standard solutions of NH_4Cl stained with indophenol blue indicator after incubation in the dark for 2 h.

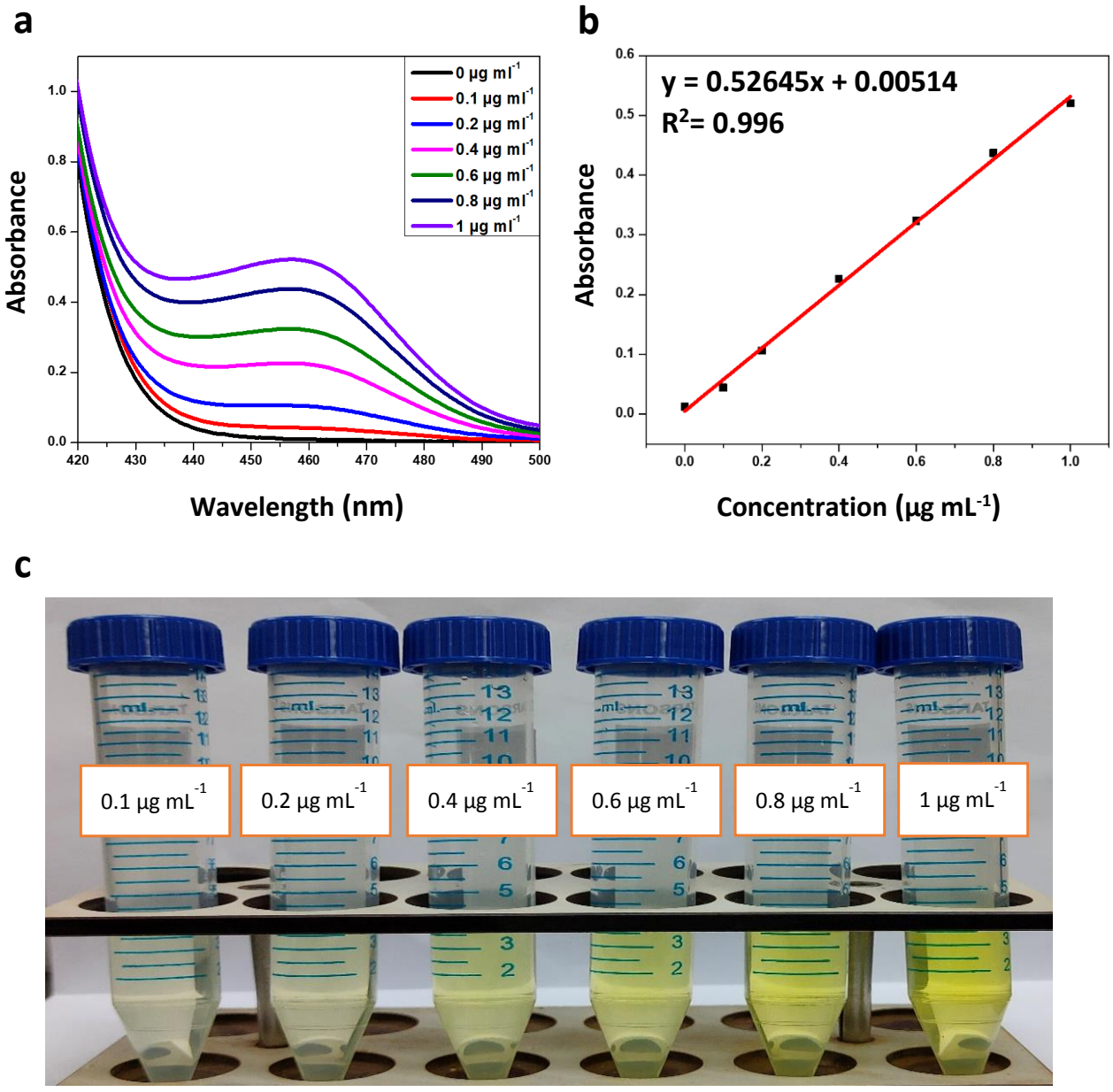

Figure S10. (a) UV-visible spectrum of known standard solution of Hydrazine monohydrate, (b) Calibration plot for N_2H_4 detection, (c) Photograph of standard solutions of Hydrazine monohydrate stained with indicator after incubation in the dark for 30 min.

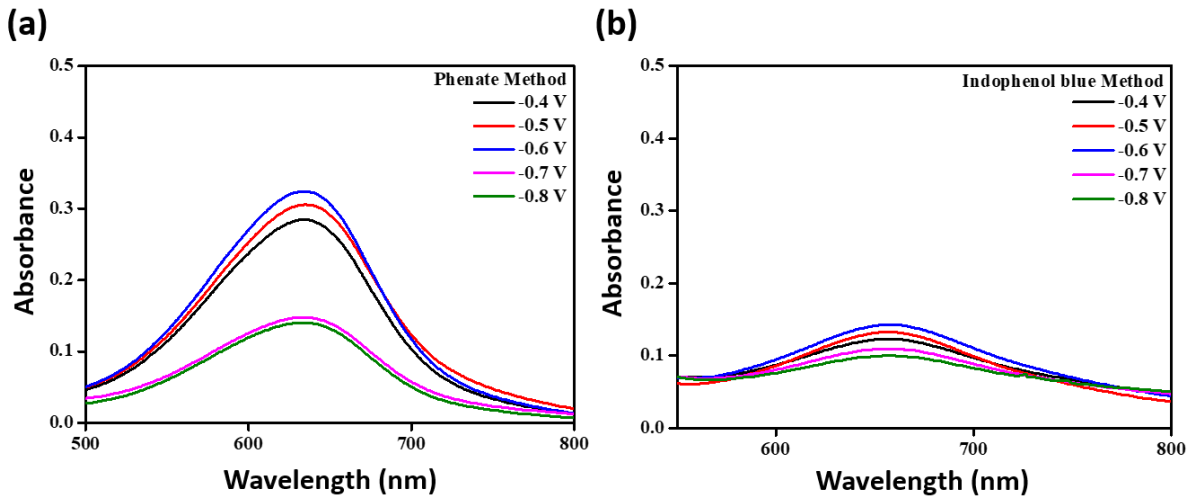

Figure S11. (a) UV-visible spectra of the stained electrolytes after 2 h electrolysis at different potentials by phenate method and (b) UV-Vis spectra of the stained electrolytes after 2 h electrolysis at different potentials by indophenol blue method.

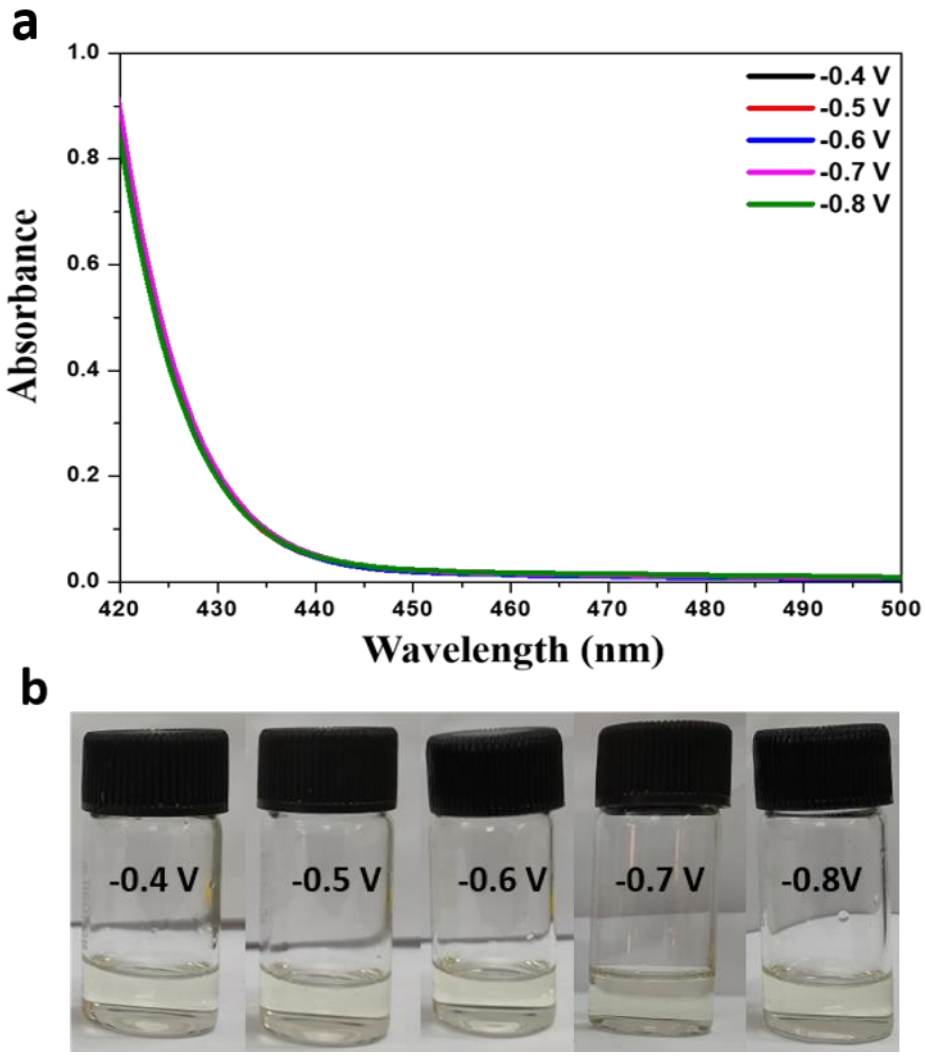

Figure S12. (a) UV-visible spectra of resultant electrolytes after 2 h of electrolysis at different potentials stained with the indicator for hydrazine detection, (b) Photograph of corresponding electrolytes stained with indicator after incubation in the dark for 30 min.

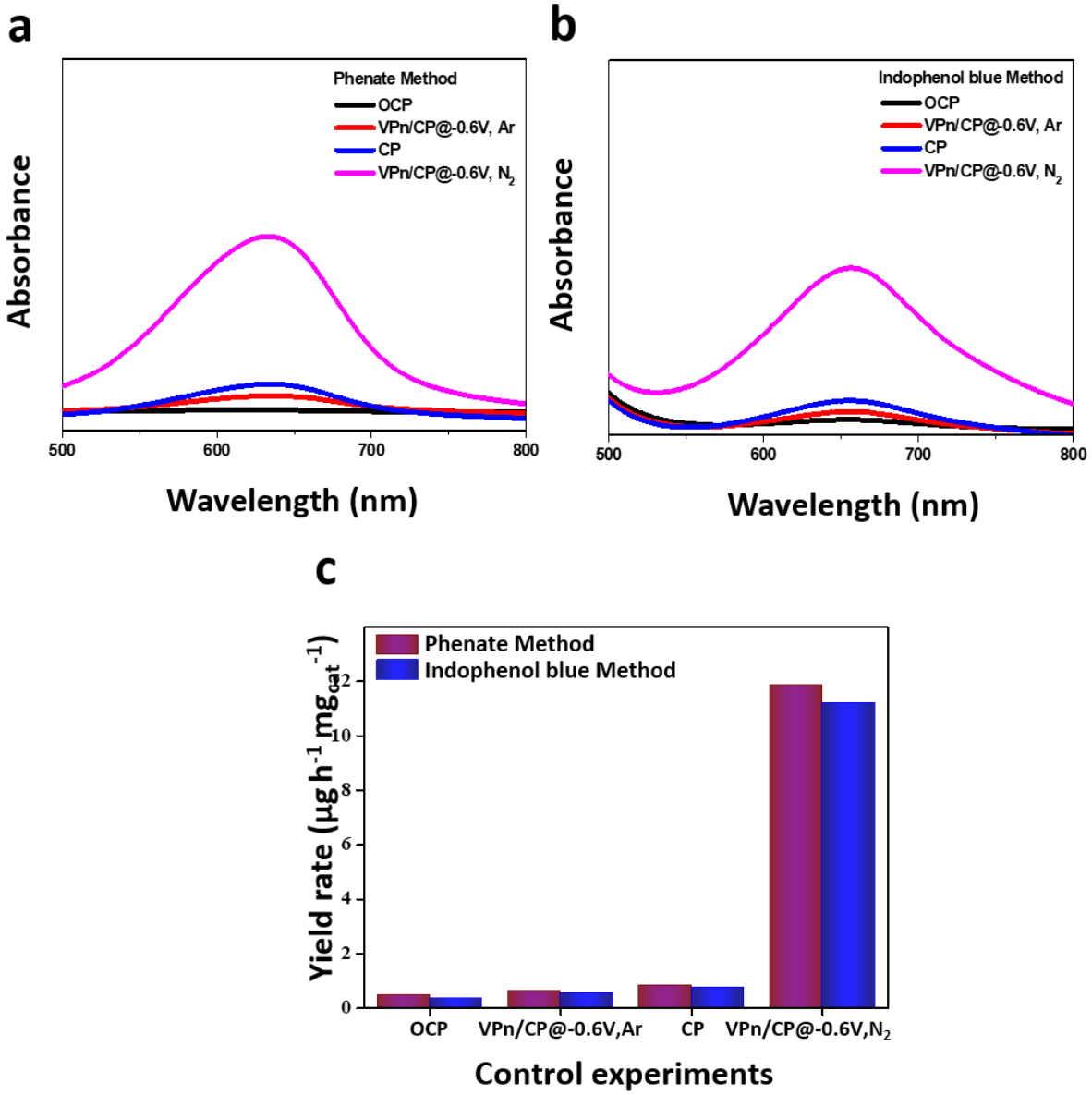

Figure S13. (a,b) UV-visible spectra of the electrolyte after electrolysis in different control experiments (at open circuit potential (OCP), with Ar feed gas at -0.6 V for 7200 s on the VPn loaded CP (VPn/CP@-0.6V, Ar), with N_2 feed gas at -0.6 V for 7200 s on the bare Carbon paper (CP), and at -0.6 V with VPn modified CP in N_2 saturated electrolyte (VPn/CP@-0.6V, N_2) , (c) Yield rate of NH_3 at four different control experiments.

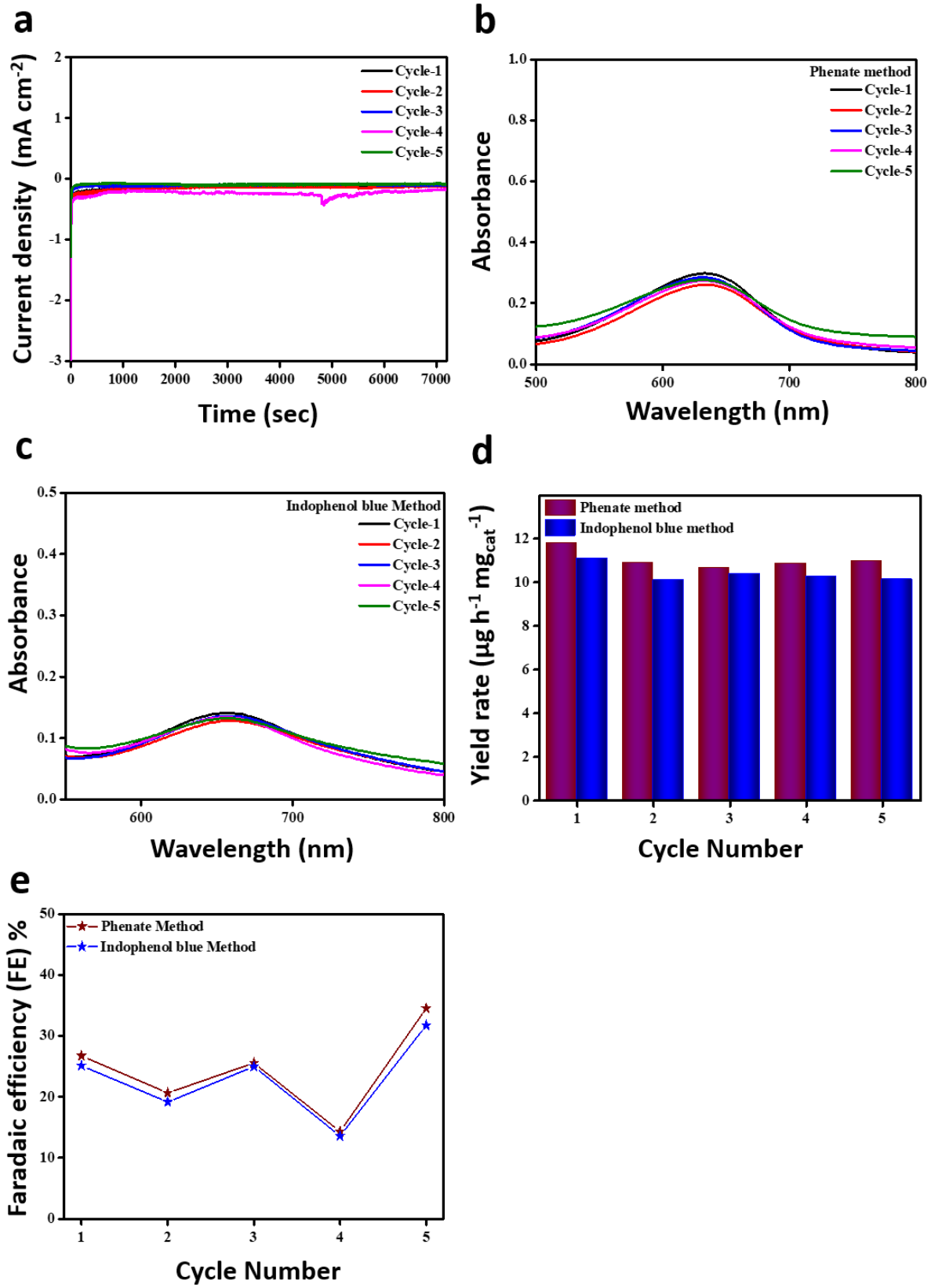

Figure S14. (a) chronoamperometry (i-t) curve of five consecutive cyclic tests of VPn at -0.6 V, (b,c) UV-visible spectra of the stained electrolytes after 2 h electrolysis during five consecutive cyclic tests at -0.6 V by phenate method and indophenol blue method respectively, (d) Yield rate of NH_3 and (e) faradaic efficiency (FE) calculated for five consecutive cyclic tests of VPn at -0.6 V.

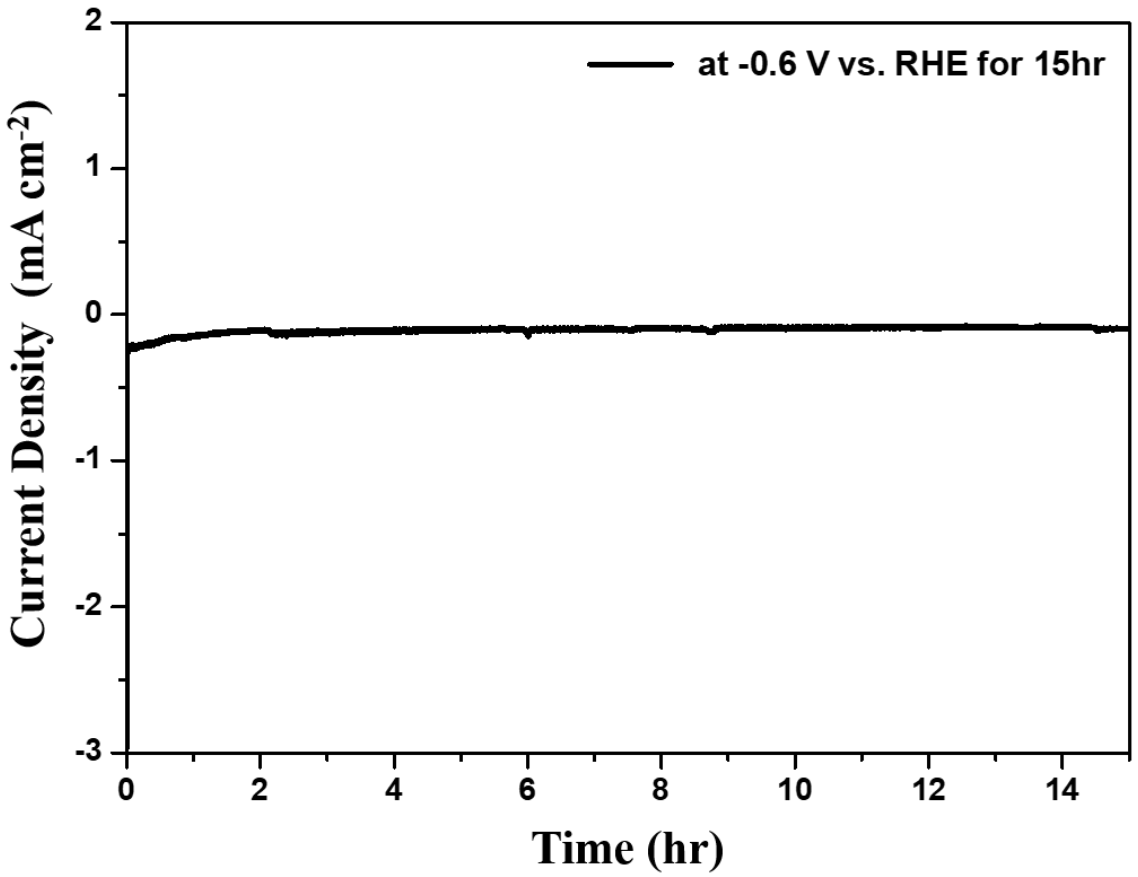

Figure S15. Long-term stability test of VPn over 15 h of electrochemical NRR.

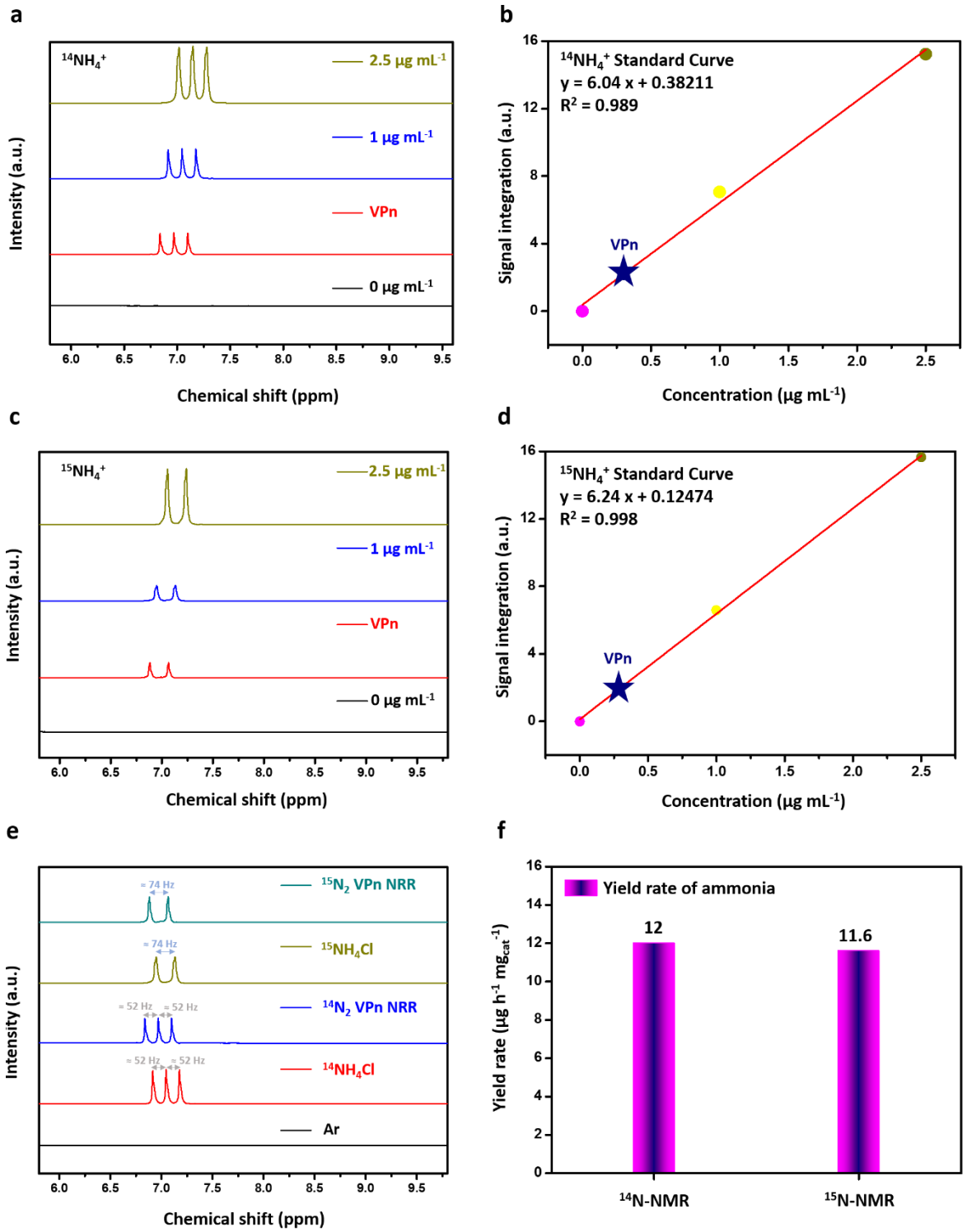

Figure S16. (a) ^{1}H-NMR spectrum acquired after isotope labeling NRR experiment by VPn for $^{14}N_2$ as feed gas compared with standard $^{14}NH_4Cl$ solutions, (b) corresponding standard calibration curve extracted from the ^{1}H-NMR spectrum, (c) ^{1}H-NMR spectrum acquired after isotope labeling NRR experiment by VPn for $^{15}N_2$ as feed gas compared with standard $^{15}NH_4Cl$ solutions, (d) corresponding standard calibration curve extracted from ^{1}H-NMR spectrum, (e) ^{1}H-NMR spectrum acquired after the NRR experiment by VPn under different gas-supply (Ar/$^{14}N_2$/$^{15}N_2$) saturated electrolyte solutions compared with standard $^{14}NH_4Cl$ and $^{15}NH_4Cl$ solution and (f) Bar diagram comparison of $^{14}NH_4^+$ and $^{15}NH_4^+$ yield rates obtained using NMR quantification method.

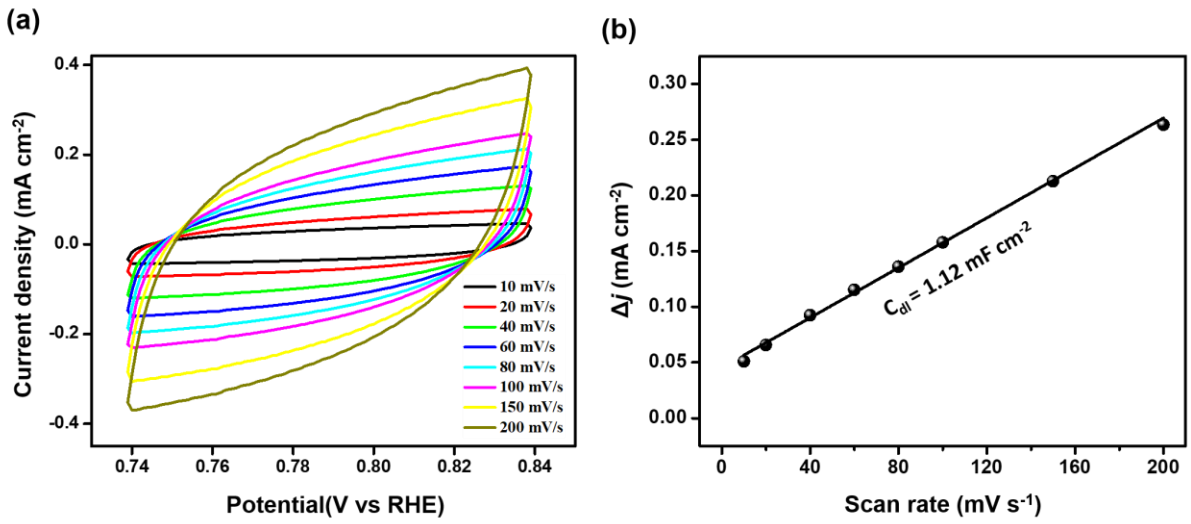

Figure S17. (a) CV curves in the non-Faradaic region at various scan rates (from 10 to 200 mV s^{-1}) for VPn material in 0.1M Na_2SO_4, (b) the corresponding fitted plot of scan rate vs. the anodic and cathodic current difference.

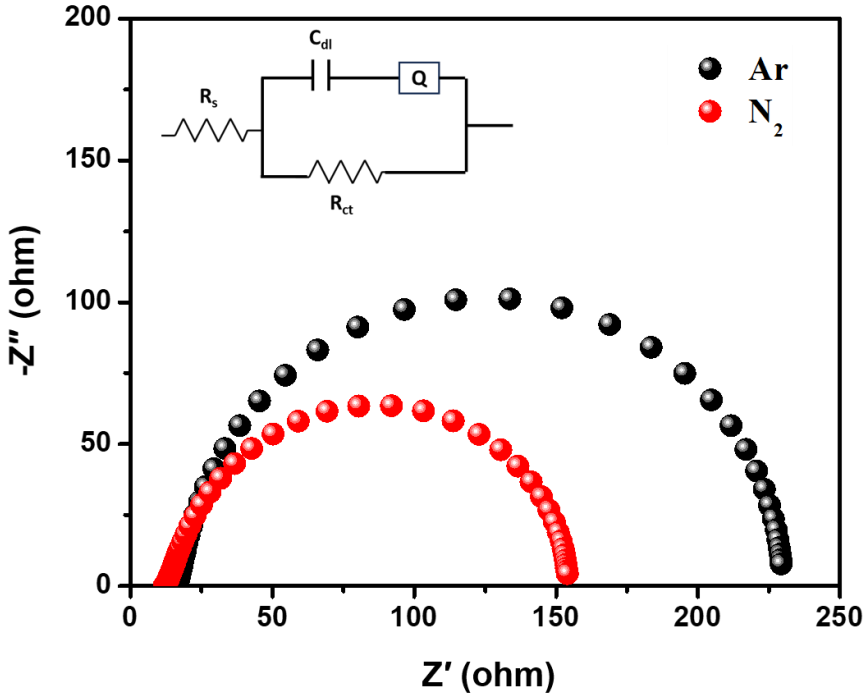

Figure S18. Nyquist plot for the electrochemical impedance measurements of the VPn material in N_2 and Ar saturated electrolyte at -0.6 V vs. RHE with a fitted equivalent circuit in the inset.

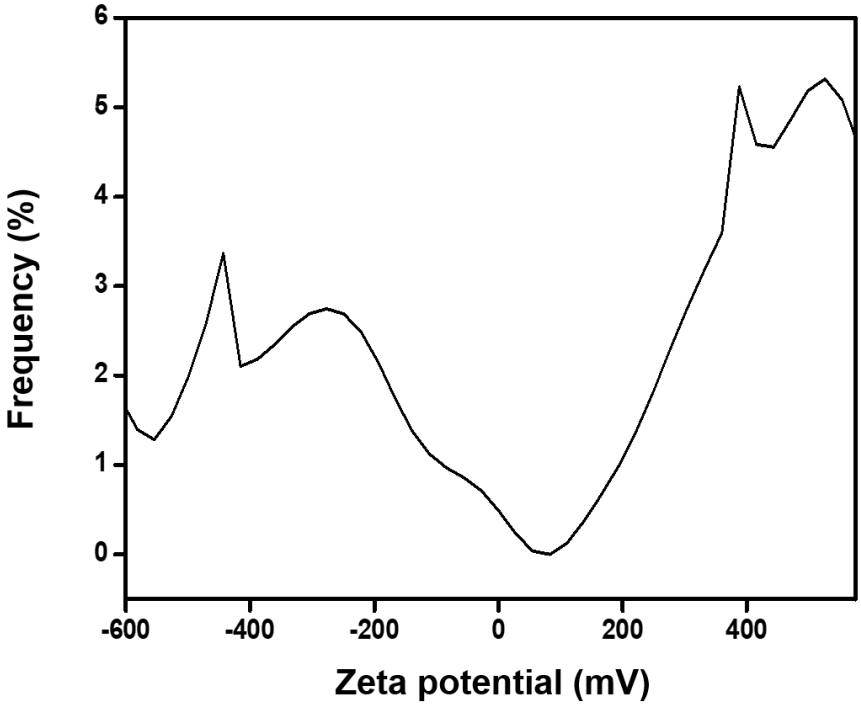

Figure S19. Zeta potential distribution curve for VPn material.

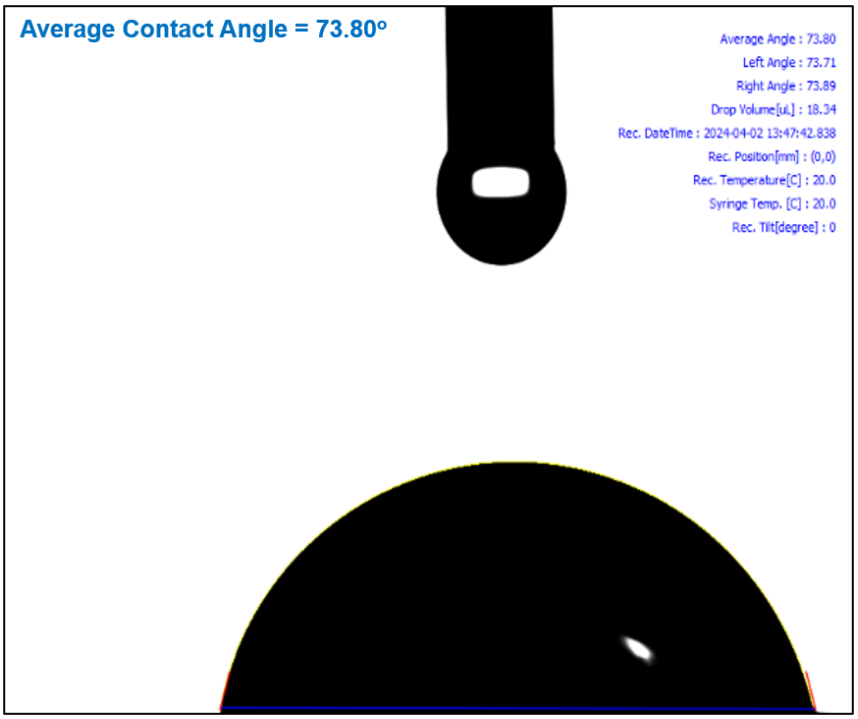

Figure S20. Surface contact angle measurement of VPn material.

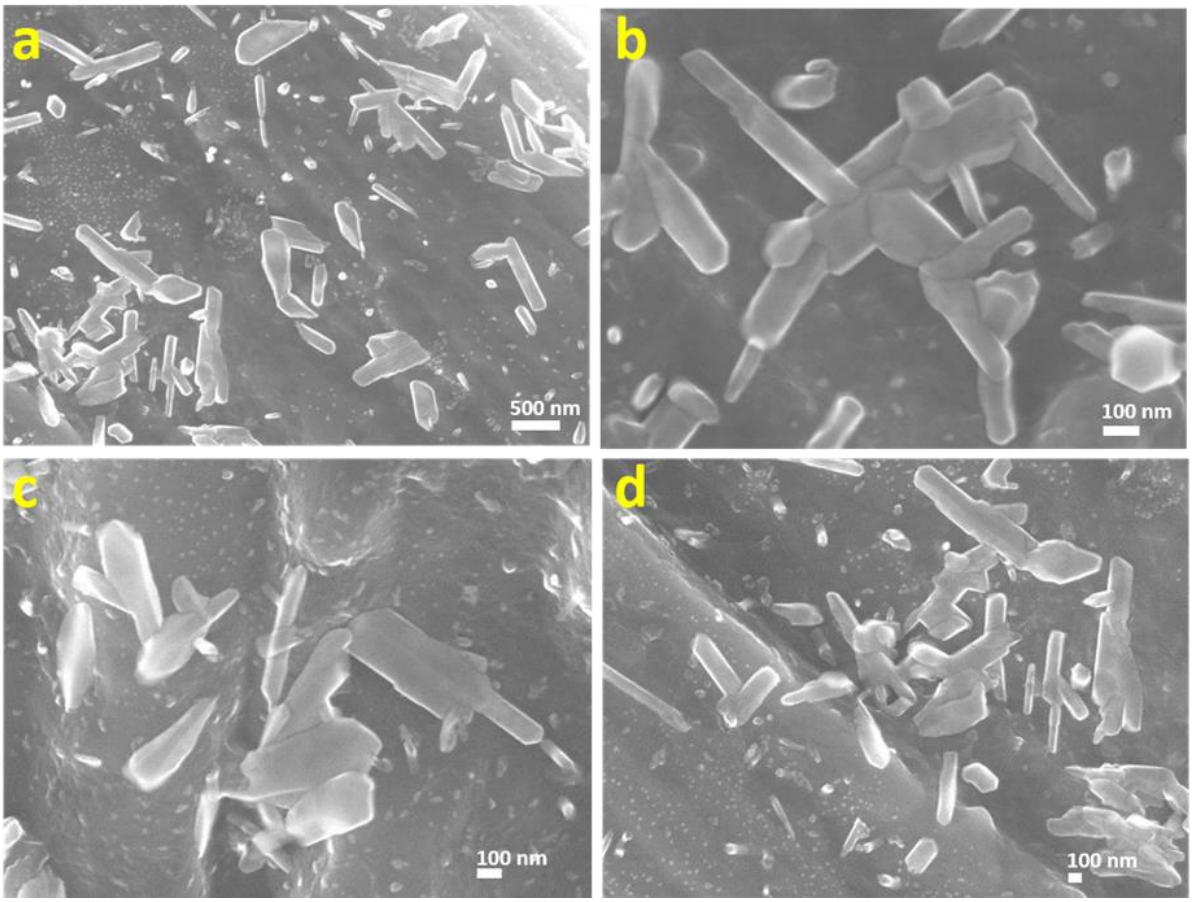

Figure S21. (a-d) FE-SEM images of VPn at different scales after durability test.

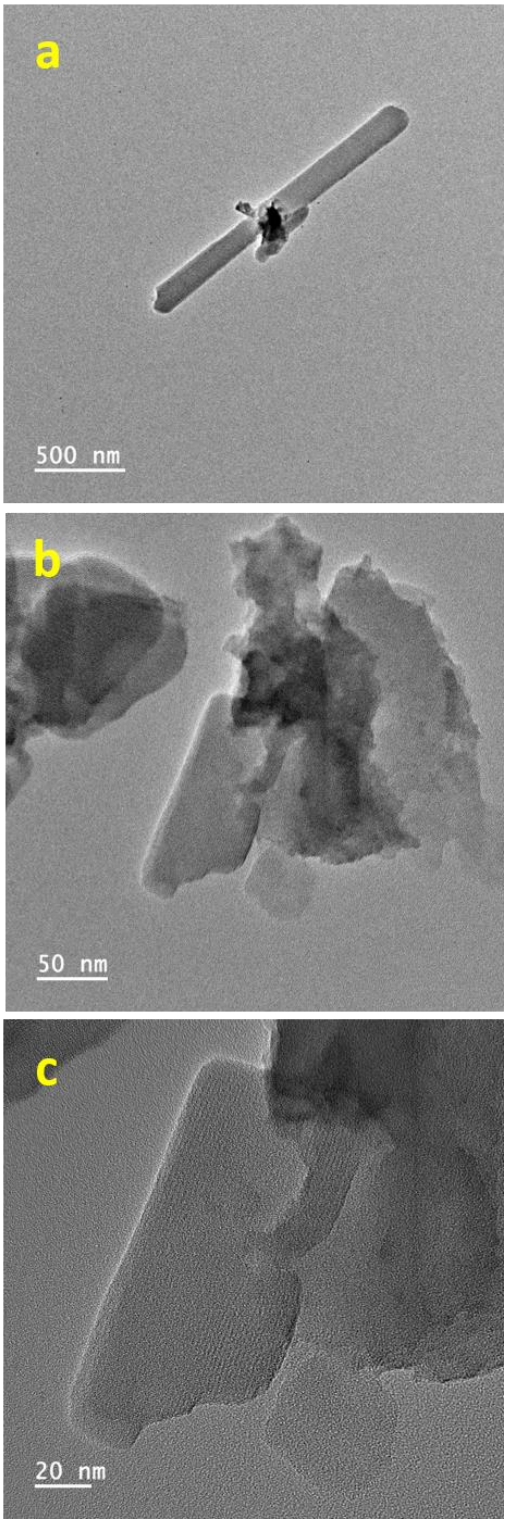

Figure S22. TEM images (a-c) of VPn catalyst after durability test.

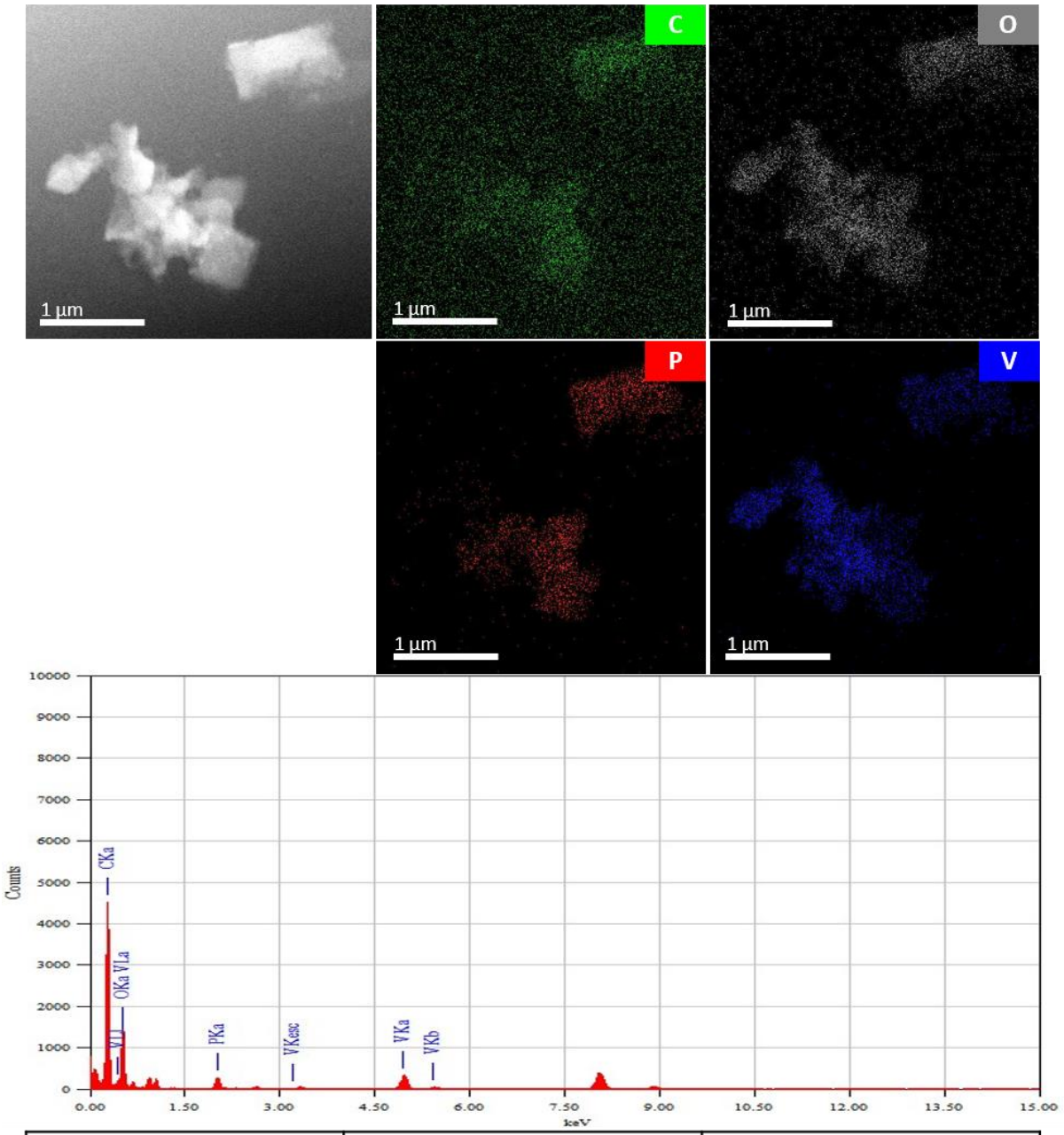

Elements	Mass %	Atom %
C	80.84	87.94
O	12.04	9.84
P	2.37	1.00
V	4.75	1.22

Figure S23. EDS and elemental mapping with corresponding TEM images of VPn catalyst after durability test.

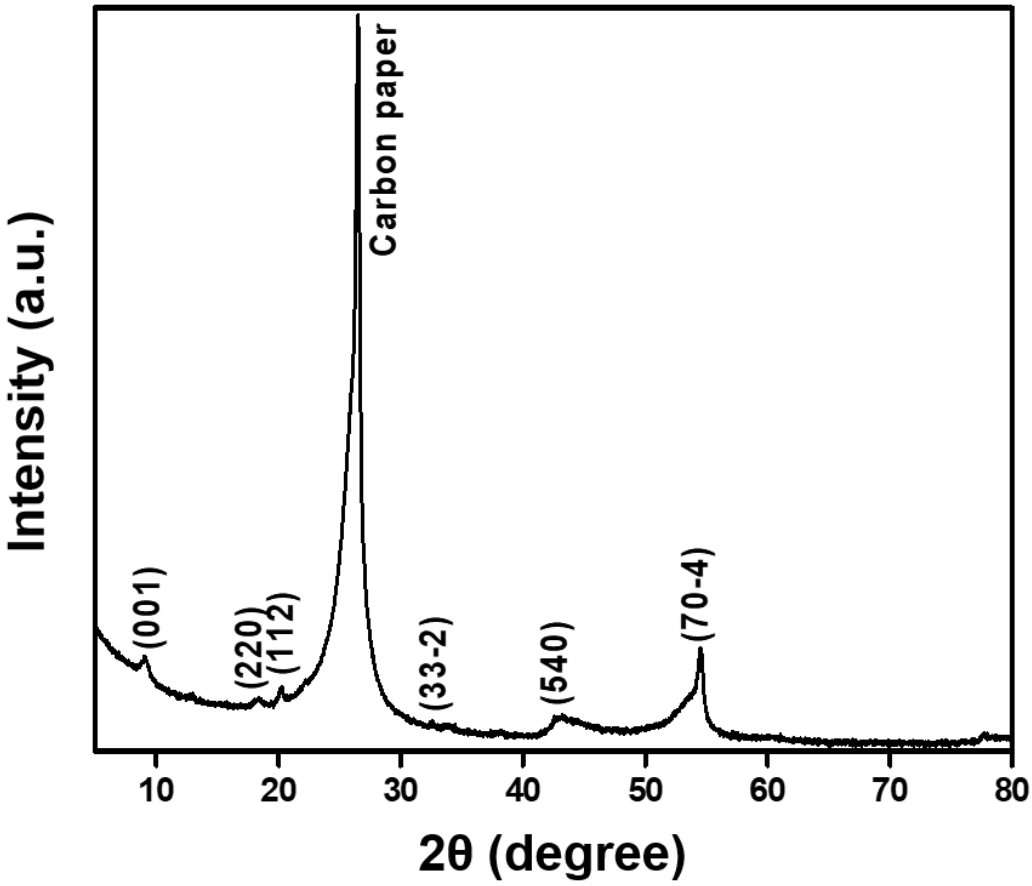

Figure S24. Wide angle powder XRD pattern of the as-prepared VPn material after a long cycling test.

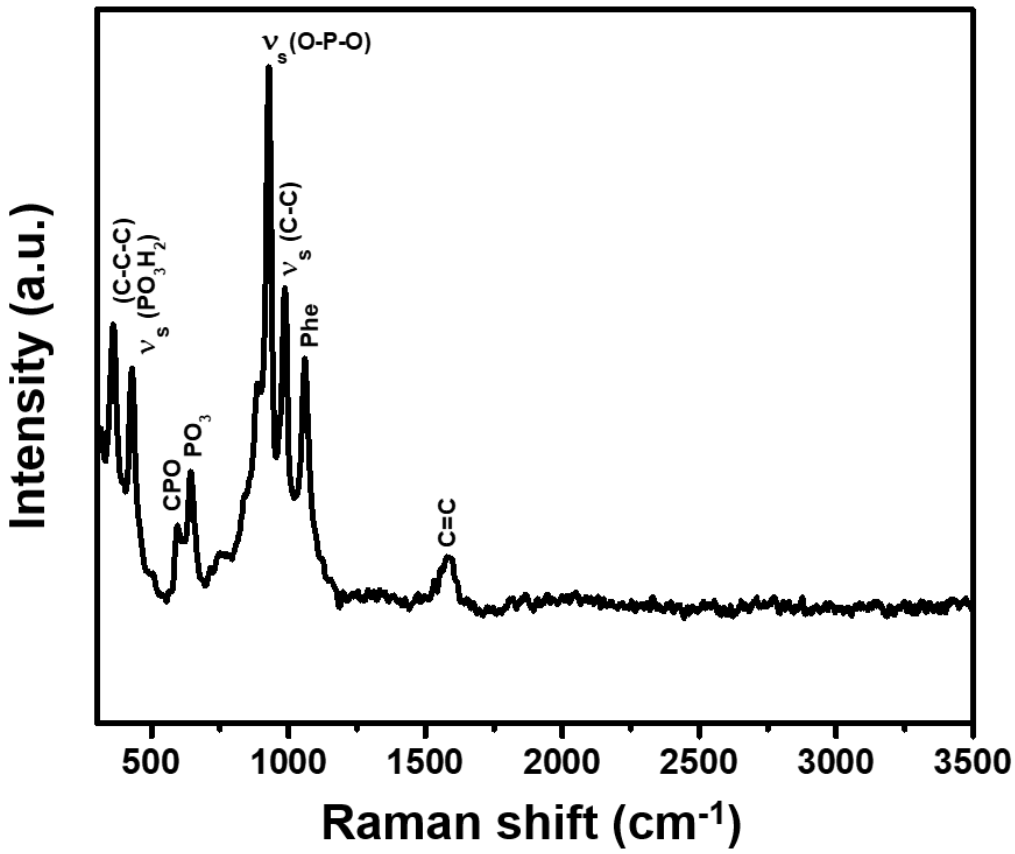

Figure S25. Raman spectrum of the as-prepared VPn material after a long cycling test.

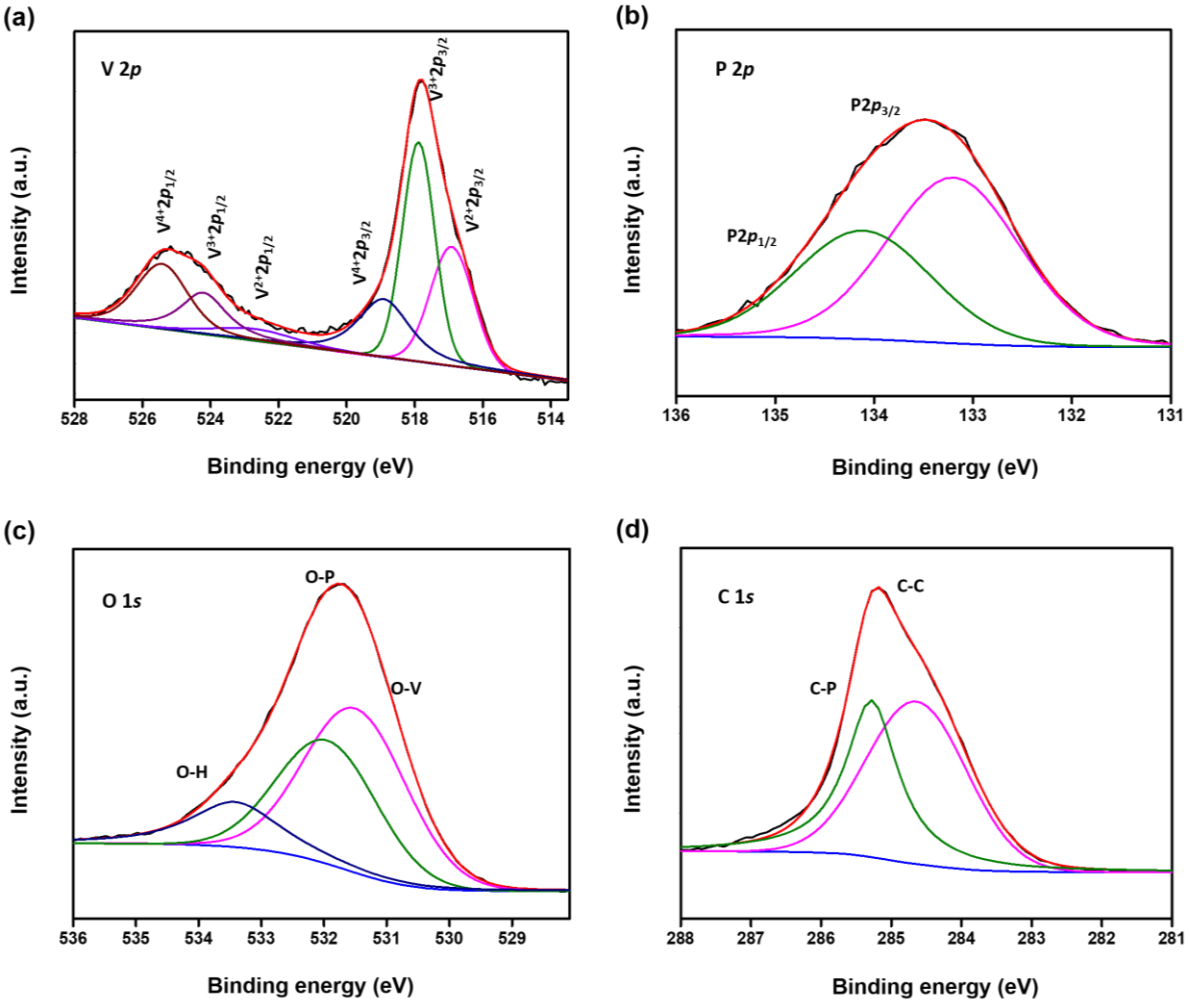

Figure S26. Narrow range XPS spectrum of VPn containing elements (a) V 2p, (b) P 2p, (c) O 1s, (d) C 1s, after a long cycling test.

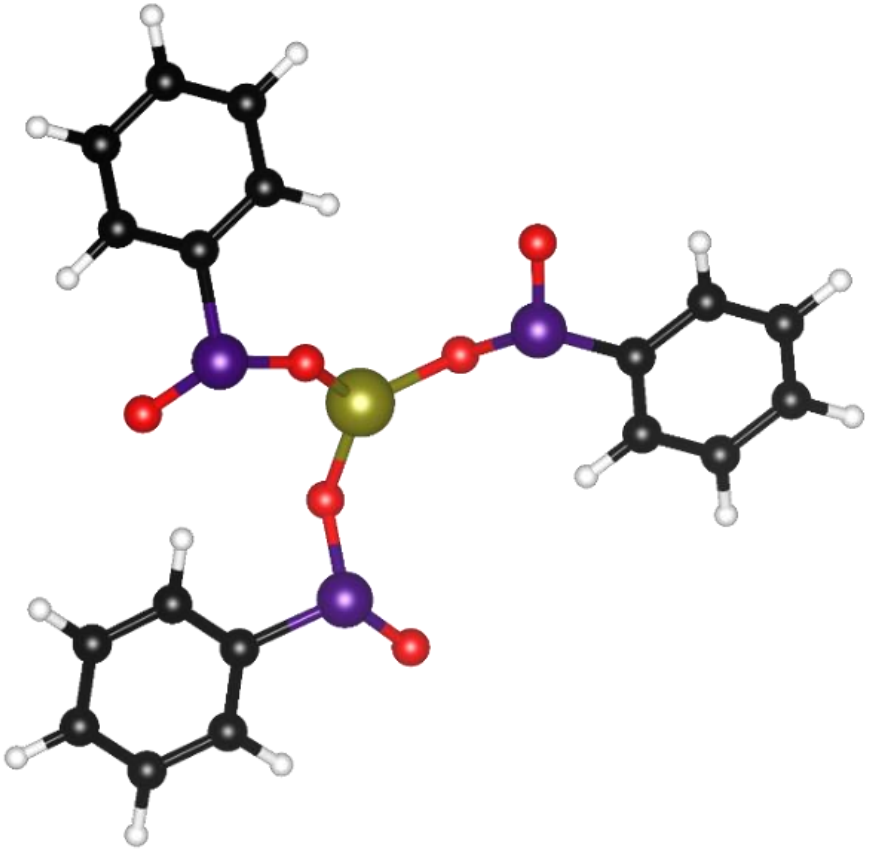

Figure S27. DFT optimized structure of as-synthesized VPn (Vanadium: Dark yellow, Oxygen: Red, Phosphorus: Purple, Carbon: Black, Hydrogen: White).

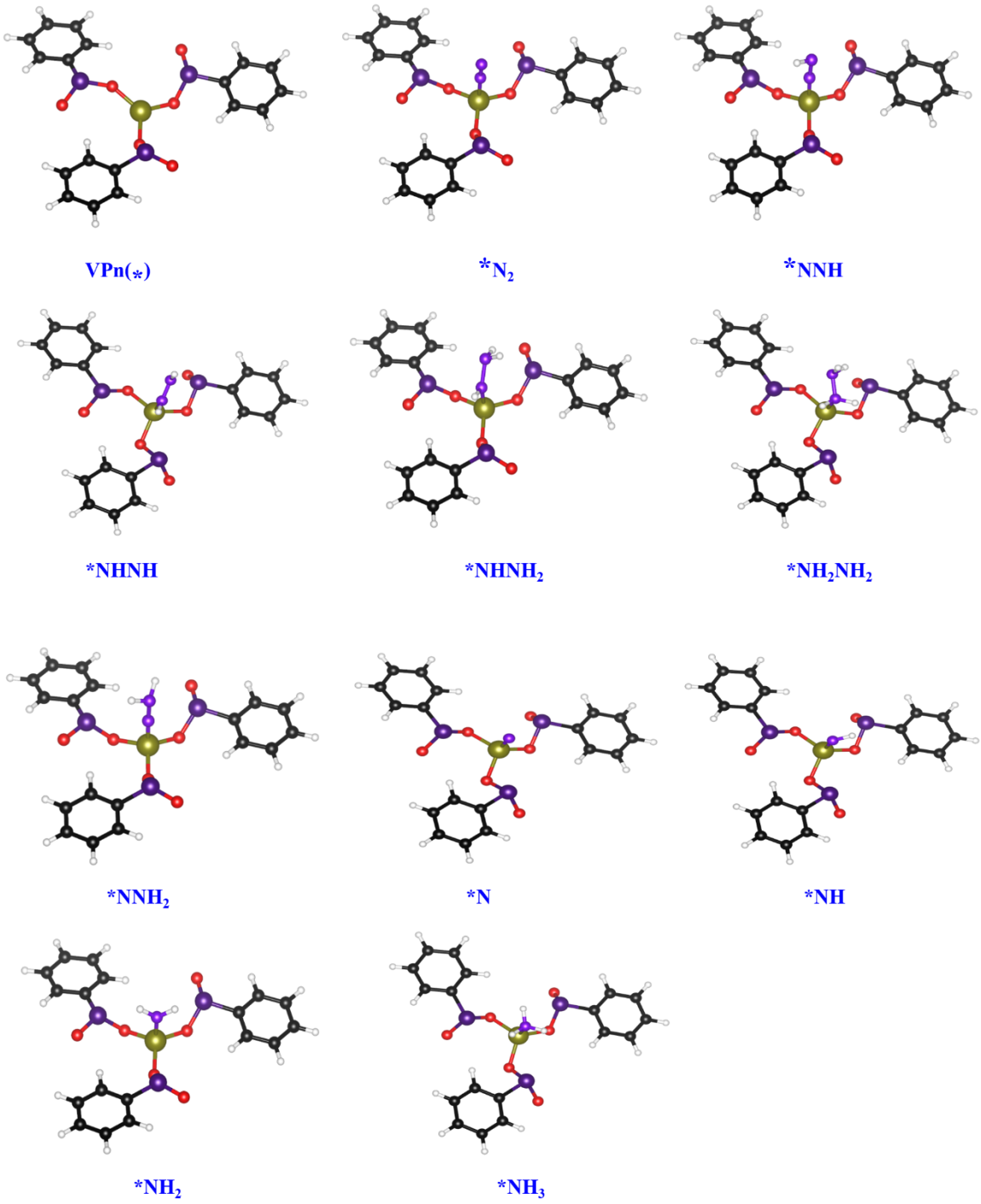

Figure S28. Optimized DFT structures of the as-prepared VPn material and all the intermediates involved in the NRR mechanism.

No.	Atom	Label	x	y	z
1	V	V1	11.10403	10.74840	8.41530
2	O	O1	12.74478	11.50641	7.98234
3	O	O2	9.71895	11.68154	9.20121
4	O	O3	11.03325	8.93416	8.12391
5	P	P1	13.48298	12.48467	9.04690
6	P	P2	11.29354	7.72558	9.18681
7	P	P3	8.15230	11.74912	9.56798
8	O	O4	13.13024	13.95684	9.04099
9	O	O5	12.60216	6.97131	9.09593
10	O	O6	7.25772	10.58900	9.18007
11	C	C1	15.24211	12.10751	8.91247
12	C	C2	16.15619	13.17213	9.00517
13	C	C3	15.68604	10.77503	8.82147
14	C	C4	17.52700	12.89795	8.97634
15	C	C5	17.05956	10.51581	8.80226
16	C	C6	17.97727	11.57353	8.87770
17	C	C7	9.78832	6.73092	9.10737
18	C	C8	8.53343	7.36607	9.05938
19	C	C9	9.89199	5.33001	9.17478
20	C	C10	7.37602	6.58231	9.05218
21	C	C11	7.47015	5.18407	9.09936
22	C	C12	8.72449	4.55992	9.15586
23	C	C13	7.58991	13.39193	9.06083
24	C	C14	6.19988	13.60577	8.97895
25	C	C15	8.49549	14.45358	8.87191
26	C	C16	5.71970	14.88643	8.69197
27	C	C17	6.61591	15.94489	8.48850
28	C	C18	7.99932	15.72751	8.57266
29	H	H1	10.88456	4.86598	9.21667
30	H	H2	8.79443	3.46557	9.17310
31	H	H3	6.55821	4.57464	9.09291
32	H	H4	6.39690	7.07325	9.00432
33	H	H5	8.45150	8.45872	9.02191
34	H	H6	5.51289	12.76400	9.12817
35	H	H7	9.57591	14.27767	8.94297
36	H	H8	8.69684	16.55747	8.40651
37	H	H9	6.23164	16.94713	8.26339
38	H	H10	4.63803	15.05961	8.62451
39	H	H11	14.95912	9.95538	8.76203
40	H	H12	17.41770	9.48120	8.73135
41	H	H13	19.05360	11.36392	8.85960
42	H	H14	18.24806	13.72208	9.02972
43	H	H15	15.77291	14.19666	9.07980

Table S3. Optimized coordinates of VPn material.

No.	Atom	Label	x	y	z
1	V	V1	11.22457	10.71422	8.99917
2	O	O1	12.81056	11.47872	8.48796
3	O	O2	9.73860	11.72821	8.63509
4	O	O3	11.03475	8.95842	8.54748
5	P	P1	13.63642	12.69025	9.22983
6	P	P2	11.30565	7.59586	9.43376
7	P	P3	8.35255	11.80417	9.51232
8	O	O4	13.26716	14.10856	8.84701
9	O	O5	12.59983	6.86013	9.15938
10	O	O6	7.40452	10.62602	9.38548
11	C	C1	15.37103	12.23227	9.00310
12	C	C2	16.33597	13.25644	9.02393
13	C	C3	15.75353	10.88168	8.91501
14	C	C4	17.69110	12.91978	8.94456
15	C	C5	17.11178	10.55951	8.83580
16	C	C6	18.07820	11.57489	8.86020
17	C	C7	9.78323	6.63841	9.23053
18	C	C8	8.53478	7.28588	9.17456
19	C	C9	9.87439	5.23335	9.23066
20	C	C10	7.37221	6.51198	9.10075
21	C	C11	7.45469	5.11209	9.09706
22	C	C12	8.70208	4.47399	9.15384
23	C	C13	7.67706	13.42880	9.08609
24	C	C14	6.27999	13.58987	9.04292
25	C	C15	8.53685	14.52677	8.89588
26	C	C16	5.74605	14.85851	8.79325
27	C	C17	6.59688	15.95721	8.61179
28	C	C18	7.98822	15.78995	8.65376
29	H	H1	10.86135	4.75750	9.27265
30	H	H2	8.76117	3.37841	9.13476
31	H	H3	6.53782	4.51250	9.04888
32	H	H4	6.39735	7.01107	9.04547
33	H	H5	8.46195	8.38024	9.18209
34	H	H6	5.63323	12.71618	9.18488
35	H	H7	9.62409	14.38735	8.92453
36	H	H8	8.65006	16.64907	8.49291
37	H	H9	6.17223	16.95217	8.43272
38	H	H10	4.65918	14.99233	8.73460
39	H	H11	14.98915	10.09645	8.89273
40	H	H12	17.41694	9.50982	8.75133
41	H	H13	19.14231	11.31610	8.80915
42	H	H14	18.45067	13.71060	8.94465
43	H	H15	16.00961	14.30139	9.08316
44	N	N1	11.32209	10.69800	10.91039
45	N	N2	11.38838	10.68794	12.04942

Table S4. Optimized coordinates of $*N_2$.

No.	Atom	Label	x	y	z
1	V	V1	11.24167	10.70743	9.03365
2	O	O1	12.74903	11.60300	8.47129
3	O	O2	9.67388	11.54255	8.59271
4	O	O3	11.26139	8.94143	8.59382
5	P	P1	13.62762	12.72602	9.25153
6	P	P2	11.37893	7.61903	9.56052
7	P	P3	8.34724	11.67855	9.54924
8	O	O4	13.29302	14.17979	9.00805
9	O	O5	12.64276	6.79787	9.43177
10	O	O6	7.34613	10.53985	9.49886
11	C	C1	15.34919	12.24781	9.00681
12	C	C2	16.31726	13.26968	9.00787
13	C	C3	15.72572	10.89224	8.94934
14	C	C4	17.66979	12.92710	8.93036
15	C	C5	17.08276	10.56520	8.87581
16	C	C6	18.05084	11.57961	8.86705
17	C	C7	9.83012	6.72248	9.29889
18	C	C8	8.60128	7.40682	9.25049
19	C	C9	9.88177	5.31645	9.26301
20	C	C10	7.41742	6.66998	9.14414
21	C	C11	7.46242	5.26992	9.08277
22	C	C12	8.69027	4.59500	9.14079
23	C	C13	7.69820	13.31323	9.13623
24	C	C14	6.30490	13.49508	9.08487
25	C	C15	8.57869	14.39847	8.97380
26	C	C16	5.79475	14.77367	8.83479
27	C	C17	6.66714	15.85644	8.65991
28	C	C18	8.05540	15.67213	8.73260
29	H	H1	10.85585	4.81506	9.31261
30	H	H2	8.71804	3.49910	9.09303
31	H	H3	6.53025	4.69888	8.99451
32	H	H4	6.45564	7.19710	9.11458
33	H	H5	8.55166	8.50086	9.29300
34	H	H6	5.64665	12.62954	9.22318
35	H	H7	9.66281	14.24398	9.02871
36	H	H8	8.73228	16.52515	8.59956
37	H	H9	6.25982	16.85698	8.47122
38	H	H10	4.71063	14.92965	8.77442
39	H	H11	14.96149	10.10648	8.95642
40	H	H12	17.39031	9.51334	8.82828
41	H	H13	19.11390	11.31597	8.81680
42	H	H14	18.43434	13.71371	8.92204
43	H	H15	15.98858	14.31479	9.05602
44	N	N1	11.26667	10.73429	10.75327
45	N	N2	11.37318	10.80958	11.99450
46	H	H16	10.65143	10.21198	12.47369

Table S5. Optimized coordinates of *NNH.

No.	Atom	Label	x	y	z
1	V	V1	11.20108	10.63275	9.27494
2	O	O1	13.04120	10.95353	8.65423
3	O	O2	10.04188	12.11694	8.71197
4	O	O3	10.54739	8.97729	8.43555
5	P	P1	13.56776	12.38082	9.49148
6	P	P2	11.21275	7.68920	9.39124
7	P	P3	8.51039	11.76769	9.45464
8	O	O4	13.39102	13.38744	8.08802
9	O	O5	11.99758	6.97351	8.01757
10	O	O6	7.85039	11.05170	8.01729
11	C	C1	15.37580	12.09078	9.24441
12	C	C2	16.24596	13.18920	9.17998
13	C	C3	15.89862	10.79084	9.13267
14	C	C4	17.61844	12.99256	8.99638
15	C	C5	17.27167	10.59796	8.94924
16	C	C6	18.13087	11.69773	8.87969
17	C	C7	9.70894	6.62338	9.29979
18	C	C8	8.42427	7.18999	9.33655
19	C	C9	9.84529	5.23034	9.20583
20	C	C10	7.29244	6.37158	9.26869
21	C	C11	7.43561	4.98496	9.16833
22	C	C12	8.71129	4.41465	9.13858
23	C	C13	7.74577	13.42267	9.15972
24	C	C14	6.34827	13.52485	9.09707
25	C	C15	8.52854	14.58060	9.01196
26	C	C16	5.73998	14.76497	8.88005
27	C	C17	6.52376	15.91174	8.72821
28	C	C18	7.91658	15.81956	8.79545
29	H	H1	10.82797	4.77665	9.18346
30	H	H2	8.82154	3.34057	9.06368
31	H	H3	6.55871	4.35278	9.11583
32	H	H4	6.30431	6.81254	9.29468
33	H	H5	8.29506	8.26143	9.41798
34	H	H6	5.73063	12.64335	9.21472
35	H	H7	9.60778	14.53446	9.06572
36	H	H8	8.52261	16.70908	8.68118
37	H	H9	6.05204	16.87133	8.56073
38	H	H10	4.66118	14.83671	8.83041
39	H	H11	15.25264	9.92495	9.18852
40	H	H12	17.66976	9.59517	8.86199
41	H	H13	19.19316	11.54645	8.73761
42	H	H14	18.28474	13.84393	8.94488
43	H	H15	15.86102	14.19707	9.27010
44	N	N1	11.13785	10.47915	11.30976
45	N	N2	11.49552	11.43927	12.01651
46	H	H16	11.46164	11.37560	13.04472
47	H	H17	10.79879	9.60953	11.74600

Table S6. Optimized coordinates of *NHNH.

No.	Atom	Label	x	y	z
1	V	V1	11.18839	10.64306	8.97150
2	O	O1	12.83673	11.39736	8.66204
3	O	O2	9.73486	11.69012	8.60056
4	O	O3	11.06754	8.88839	8.44485
5	P	P1	13.64797	12.49541	9.56041
6	P	P2	11.28955	7.55438	9.37455
7	P	P3	8.36131	11.75035	9.49308
8	O	O4	13.21675	13.94497	9.42595
9	O	O5	12.55861	6.75894	9.14834
10	O	O6	7.38719	10.59515	9.35594
11	C	C1	15.38440	12.14888	9.20008
12	C	C2	16.29180	13.22024	9.10677
13	C	C3	15.83452	10.81675	9.13941
14	C	C4	17.65259	12.95089	8.92442
15	C	C5	17.19761	10.56099	8.96850
16	C	C6	18.10469	11.62556	8.85926
17	C	C7	9.74617	6.62998	9.20132
18	C	C8	8.50596	7.29562	9.19831
19	C	C9	9.81744	5.22484	9.18836
20	C	C10	7.33123	6.53771	9.16704
21	C	C11	7.39480	5.13697	9.14818
22	C	C12	8.63393	4.48139	9.15197
23	C	C13	7.68177	13.38203	9.11722
24	C	C14	6.28359	13.52590	9.07914
25	C	C15	8.52750	14.49686	8.97415
26	C	C16	5.73240	14.79345	8.86839
27	C	C17	6.56884	15.90739	8.71846
28	C	C18	7.96232	15.75947	8.77168
29	H	H1	10.80120	4.74119	9.18767
30	H	H2	8.67649	3.38596	9.12068
31	H	H3	6.46977	4.54903	9.12716
32	H	H4	6.35981	7.04606	9.15439
33	H	H5	8.44407	8.39118	9.21225
34	H	H6	5.65323	12.63757	9.20053
35	H	H7	9.61633	14.37097	9.01319
36	H	H8	8.61122	16.63537	8.65480
37	H	H9	6.12986	16.89957	8.55717
38	H	H10	4.64375	14.91405	8.81863
39	H	H11	15.12030	9.98853	9.22358
40	H	H12	17.55955	9.52663	8.92188
41	H	H13	19.17393	11.41861	8.73132
42	H	H14	18.36952	13.77732	8.83368
43	H	H15	15.91710	14.24915	9.16683
44	N	N1	11.07304	10.46856	10.78602
45	N	N2	11.27103	11.41855	11.81472
46	H	H16	11.99565	11.07336	12.47030
47	H	H17	10.74277	9.57780	11.20230
48	H	H18	11.61592	12.29999	11.39446

Table S7. Optimized coordinates of *$NHNH_2$.

No.	Atom	Label	x	y	z
1	V	V1	11.22378	10.62875	9.40900
2	O	O1	13.07441	10.87231	8.78373
3	O	O2	10.11218	12.16407	8.88650
4	O	O3	10.50543	9.01948	8.53696
5	P	P1	13.60738	12.36893	9.48301
6	P	P2	11.19687	7.68815	9.41118
7	P	P3	8.53386	11.77387	9.49973
8	O	O4	13.40698	13.26129	8.00735
9	O	O5	11.94581	7.03430	7.98766
10	O	O6	7.98424	11.08460	8.00443
11	C	C1	15.41674	12.07763	9.23637
12	C	C2	16.28188	13.18002	9.17078
13	C	C3	15.94678	10.77985	9.12390
14	C	C4	17.65543	12.99028	8.98770
15	C	C5	17.32095	10.59441	8.94097
16	C	C6	18.17447	11.69827	8.87186
17	C	C7	9.69468	6.62095	9.31102
18	C	C8	8.40765	7.18297	9.34339
19	C	C9	9.83638	5.22877	9.21328
20	C	C10	7.27936	6.36098	9.26772
21	C	C11	7.42776	4.97534	9.16378
22	C	C12	8.70546	4.40941	9.13829
23	C	C13	7.75794	13.42173	9.19266
24	C	C14	6.35994	13.50672	9.11785
25	C	C15	8.52792	14.58870	9.04464
26	C	C16	5.73844	14.73812	8.88964
27	C	C17	6.50926	15.89335	8.73773
28	C	C18	7.90232	15.81863	8.81653
29	H	H1	10.82116	4.77901	9.19358
30	H	H2	8.81973	3.33598	9.06069
31	H	H3	6.55326	4.34065	9.10541
32	H	H4	6.28998	6.79890	9.29060
33	H	H5	8.27260	8.25332	9.42778
34	H	H6	5.75233	12.61777	9.23510
35	H	H7	9.60721	14.55807	9.10654
36	H	H8	8.49856	16.71426	8.70195
37	H	H9	6.02750	16.84576	8.56109
38	H	H10	4.65942	14.79587	8.83106
39	H	H11	15.30774	9.90904	9.17889
40	H	H12	17.72418	9.59395	8.85471
41	H	H13	19.23738	11.55259	8.73158
42	H	H14	18.31707	13.84523	8.93696
43	H	H15	15.89127	14.18617	9.25986
44	N	N1	11.16486	10.40903	11.45268
45	N	N2	10.90849	11.66619	12.02425
46	H	H16	10.92627	11.56970	13.06623
47	H	H17	10.38676	9.76090	11.71427
48	H	H18	11.67559	12.31699	11.74245
49	H	H19	12.07902	10.04248	11.80642

Table S8. Optimized coordinates of *NH_2NH_2.

No.	Atom	Label	x	y	z
1	V	V1	12.14316	11.85843	8.94865
2	O	O1	13.59463	12.80180	8.37490
3	O	O2	10.51846	12.59030	8.47875
4	O	O3	12.17070	10.08963	8.55034
5	P	P1	14.46376	13.84118	9.31186
6	P	P2	12.29129	8.80139	9.57544
7	P	P3	9.25844	12.79713	9.50749
8	O	O4	14.15458	15.31632	9.15551
9	O	O5	13.55021	7.97075	9.44121
10	O	O6	8.20152	11.70731	9.51856
11	C	C1	16.19354	13.38222	9.03047
12	C	C2	17.15226	14.41195	9.02520
13	C	C3	16.58725	12.03366	8.96193
14	C	C4	18.50832	14.08791	8.92082
15	C	C5	17.94663	11.72144	8.86386
16	C	C6	18.90520	12.74577	8.84217
17	C	C7	10.74262	7.89270	9.31988
18	C	C8	9.50808	8.56612	9.29897
19	C	C9	10.79858	6.48839	9.25161
20	C	C10	8.32700	7.82490	9.18501
21	C	C11	8.37771	6.42604	9.10044
22	C	C12	9.61051	5.75918	9.13014
23	C	C13	8.63256	14.44677	9.10861
24	C	C14	7.24185	14.64433	9.08611
25	C	C15	9.51787	15.52352	8.92536
26	C	C16	6.73492	15.92239	8.83463
27	C	C17	7.61182	16.99704	8.62919
28	C	C18	8.99997	16.79980	8.68537
29	H	H1	11.77241	5.98757	9.27520
30	H	H2	9.64629	4.66501	9.05376
31	H	H3	7.44799	5.85118	9.00789
32	H	H4	7.36499	8.35080	9.16027
33	H	H5	9.44762	9.65818	9.36559
34	H	H6	6.58236	13.78372	9.24608
35	H	H7	10.60119	15.35865	8.96285
36	H	H8	9.68528	17.64380	8.54378
37	H	H9	7.21373	17.99869	8.42880
38	H	H10	5.64955	16.07743	8.79941
39	H	H11	15.83399	11.23688	8.97814
40	H	H12	18.25868	10.67191	8.80494
41	H	H13	19.96961	12.49294	8.76943
42	H	H14	19.25762	14.88867	8.89772
43	H	H15	16.81619	15.45308	9.08462
44	N	N1	12.17063	11.96592	10.59369
45	N	N2	12.23527	12.06577	11.92880
46	H	H16	11.40193	11.68368	12.40264
47	H	H17	12.49726	13.01261	12.24658

Table S9. Optimized coordinates of *NNH_2.

No.	Atom	Label	x	y	z
1	V	V1	11.16627	10.73557	9.08938
2	O	O1	12.96590	11.12350	8.39422
3	O	O2	9.93015	12.13837	8.47638
4	O	O3	10.56864	9.00566	8.35844
5	P	P1	13.48934	12.54075	9.25282
6	P	P2	11.22365	7.79693	9.42151
7	P	P3	8.42186	11.78402	9.26433
8	O	O4	13.44086	13.53550	7.83027
9	O	O5	12.07060	7.01361	8.12308
10	O	O6	7.70617	11.12259	7.82690
11	C	C1	15.29581	12.17714	9.12952
12	C	C2	16.21170	13.23876	9.08692
13	C	C3	15.77097	10.85522	9.09111
14	C	C4	17.58377	12.98322	8.99670
15	C	C5	17.14354	10.60337	9.00093
16	C	C6	18.04934	11.66628	8.95218
17	C	C7	9.73696	6.70659	9.34559
18	C	C8	8.44739	7.25991	9.39238
19	C	C9	9.88718	5.31452	9.25399
20	C	C10	7.32324	6.43017	9.33687
21	C	C11	7.47958	5.04480	9.23879
22	C	C12	8.76073	4.48730	9.19911
23	C	C13	7.68392	13.46321	9.04383
24	C	C14	6.28885	13.59661	8.98369
25	C	C15	8.49014	14.61067	8.94884
26	C	C16	5.70685	14.85785	8.82085
27	C	C17	6.51437	15.99391	8.72071
28	C	C18	7.90467	15.87027	8.78626
29	H	H1	10.87374	4.86992	9.22462
30	H	H2	8.88105	3.41415	9.12608
31	H	H3	6.60862	4.40374	9.19567
32	H	H4	6.33103	6.86136	9.37041
33	H	H5	8.31025	8.33073	9.47148
34	H	H6	5.65282	12.72383	9.06131
35	H	H7	9.56812	14.53970	9.00229
36	H	H8	8.52953	16.75096	8.71210
37	H	H9	6.06334	16.96966	8.59461
38	H	H10	4.62990	14.95452	8.77254
39	H	H11	15.08724	10.01784	9.13263
40	H	H12	17.50478	9.58352	8.96973
41	H	H13	19.11126	11.46929	8.88218
42	H	H14	18.28602	13.80605	8.96154
43	H	H15	15.86301	14.26317	9.12190
44	N	N1	11.19289	10.69579	10.80031

Table S10. Optimized coordinates of *N.

No.	Atom	Label	x	y	z
1	V	V1	11.16071	10.71763	9.15526
2	O	O1	12.97824	11.04861	8.47746
3	O	O2	9.97096	12.16997	8.56967
4	O	O3	10.50299	9.02261	8.39947
5	P	P1	13.47945	12.52881	9.23669
6	P	P2	11.18785	7.77962	9.40105
7	P	P3	8.44033	11.80757	9.30812
8	O	O4	13.42941	13.42785	7.75188
9	O	O5	11.98317	7.03083	8.05073
10	O	O6	7.76837	11.14477	7.85071
11	C	C1	15.29416	12.19115	9.15184
12	C	C2	16.19026	13.26913	9.09837
13	C	C3	15.79603	10.87813	9.15288
14	C	C4	17.56849	13.03914	9.03694
15	C	C5	17.17501	10.65190	9.09155
16	C	C6	18.06060	11.73122	9.03223
17	C	C7	9.69731	6.69283	9.34775
18	C	C8	8.40793	7.24480	9.41897
19	C	C9	9.84709	5.30134	9.24943
20	C	C10	7.28381	6.41362	9.38132
21	C	C11	7.43998	5.02864	9.27672
22	C	C12	8.72088	4.47288	9.21234
23	C	C13	7.69437	13.48067	9.07049
24	C	C14	6.29859	13.60265	9.00419
25	C	C15	8.49210	14.63353	8.96855
26	C	C16	5.70715	14.85768	8.82891
27	C	C17	6.50601	15.99923	8.72245
28	C	C18	7.89709	15.88711	8.79364
29	H	H1	10.83376	4.85844	9.20101
30	H	H2	8.84131	3.40010	9.13423
31	H	H3	6.56915	4.38644	9.24780
32	H	H4	6.29169	6.84323	9.43410
33	H	H5	8.27020	8.31508	9.50387
34	H	H6	5.66930	12.72539	9.08669
35	H	H7	9.57039	14.57218	9.02618
36	H	H8	8.51508	16.77222	8.71453
37	H	H9	6.04753	16.97030	8.58713
38	H	H10	4.62964	14.94515	8.77616
39	H	H11	15.12961	10.02761	9.20337
40	H	H12	17.55721	9.63913	9.09118
41	H	H13	19.12742	11.55407	8.98483
42	H	H14	18.25496	13.87485	8.99342
43	H	H15	15.82106	14.28698	9.10253
44	N	N1	11.17754	10.64098	11.00133
45	H	H16	12.06017	10.76565	11.51548

Table S11. Optimized coordinates of *NH.

No.	Atom	Label	x	y	z
1	V	V1	11.07710	10.69307	8.78411
2	O	O1	12.62571	11.61829	8.43258
3	O	O2	9.55501	11.63705	8.37292
4	O	O3	11.02394	8.93324	8.33795
5	P	P1	13.43743	12.63365	9.43206
6	P	P2	11.20232	7.64178	9.32078
7	P	P3	8.22294	11.74855	9.31720
8	O	O4	13.09935	14.10833	9.35289
9	O	O5	12.48120	6.84647	9.20614
10	O	O6	7.21080	10.62264	9.19416
11	C	C1	15.17549	12.21212	9.13905
12	C	C2	16.13051	13.24445	9.16042
13	C	C3	15.57462	10.87016	8.99919
14	C	C4	17.48480	12.92897	9.01623
15	C	C5	16.93304	10.56717	8.86497
16	C	C6	17.88718	11.59440	8.87384
17	C	C7	9.67526	6.68832	9.17817
18	C	C8	8.41798	7.31840	9.10429
19	C	C9	9.78511	5.28708	9.26863
20	C	C10	7.26575	6.52605	9.09259
21	C	C11	7.36927	5.12863	9.15503
22	C	C12	8.62428	4.50991	9.24390
23	C	C13	7.60020	13.41082	8.96828
24	C	C14	6.20918	13.60770	8.91419
25	C	C15	8.49052	14.49314	8.83930
26	C	C16	5.70900	14.89681	8.70670
27	C	C17	6.58944	15.97839	8.57597
28	C	C18	7.97542	15.77800	8.64044
29	H	H1	10.77811	4.82824	9.33775
30	H	H2	8.70079	3.41654	9.29516
31	H	H3	6.46224	4.51344	9.13673
32	H	H4	6.28068	7.00664	9.03724
33	H	H5	8.32669	8.41078	9.05288
34	H	H6	5.54018	12.74463	9.00651
35	H	H7	9.57371	14.32812	8.87911
36	H	H8	8.65997	16.62732	8.52781
37	H	H9	6.19281	16.98871	8.42220
38	H	H10	4.62610	15.05744	8.63877
39	H	H11	14.82507	10.07012	8.98372
40	H	H12	17.24903	9.52396	8.74755
41	H	H13	18.95126	11.35222	8.76865
42	H	H14	18.23217	13.73175	9.00869
43	H	H15	15.79500	14.28191	9.26807
44	N	N1	11.11529	10.59336	10.61800
45	H	H16	11.99025	10.63309	11.16786
46	H	H17	10.28064	10.56194	11.22748

Table S12. Optimized coordinates of *NH_2.

No.	Atom	Label	x	y	z
1	V	V1	11.07445	10.70020	8.88793
2	O	O1	12.86460	11.20014	8.24578
3	O	O2	9.77246	12.01821	8.22906
4	O	O3	10.61109	8.93400	8.15235
5	P	P1	13.34187	12.53642	9.24707
6	P	P2	11.25224	7.78554	9.28619
7	P	P3	8.32749	11.70812	9.14162
8	O	O4	13.33185	13.64097	7.90722
9	O	O5	12.06399	6.89889	8.03295
10	O	O6	7.49375	11.06987	7.75872
11	C	C1	15.15044	12.17943	9.15377
12	C	C2	16.06912	13.23833	9.09842
13	C	C3	15.62195	10.85643	9.15232
14	C	C4	17.44146	12.97746	9.03147
15	C	C5	16.99484	10.59900	9.08502
16	C	C6	17.90403	11.65858	9.02304
17	C	C7	9.73770	6.73142	9.30161
18	C	C8	8.46574	7.32151	9.37163
19	C	C9	9.84788	5.33312	9.25759
20	C	C10	7.31875	6.52185	9.38547
21	C	C11	7.43496	5.12998	9.33404
22	C	C12	8.69881	4.53605	9.27210
23	C	C13	7.64010	13.41301	8.97175
24	C	C14	6.25256	13.59558	8.87474
25	C	C15	8.48612	14.53435	8.95409
26	C	C16	5.71801	14.88184	8.75032
27	C	C17	6.56545	15.99297	8.72591
28	C	C18	7.94829	15.81926	8.82952
29	H	H1	10.82024	4.86004	9.21161
30	H	H2	8.78801	3.45796	9.23545
31	H	H3	6.54638	4.51194	9.34485
32	H	H4	6.34018	6.98114	9.43626
33	H	H5	8.36096	8.39791	9.41464
34	H	H6	5.58592	12.74285	8.89397
35	H	H7	9.55891	14.41934	9.03748
36	H	H8	8.60370	16.68034	8.81395
37	H	H9	6.15074	16.98813	8.62981
38	H	H10	4.64691	15.01726	8.67305
39	H	H11	14.93187	10.02426	9.20380
40	H	H12	17.35376	9.57797	9.08158
41	H	H13	18.96631	11.45774	8.97106
42	H	H14	18.14629	13.79765	8.98639
43	H	H15	15.72338	14.26414	9.10603
44	N	N1	11.04541	10.66501	10.94343
45	H	H16	11.94714	10.27782	11.30037
46	H	H17	10.25563	10.06732	11.27439
47	H	H18	10.91838	11.63566	11.30690

Table S13. Optimized coordinates of *NH_3.

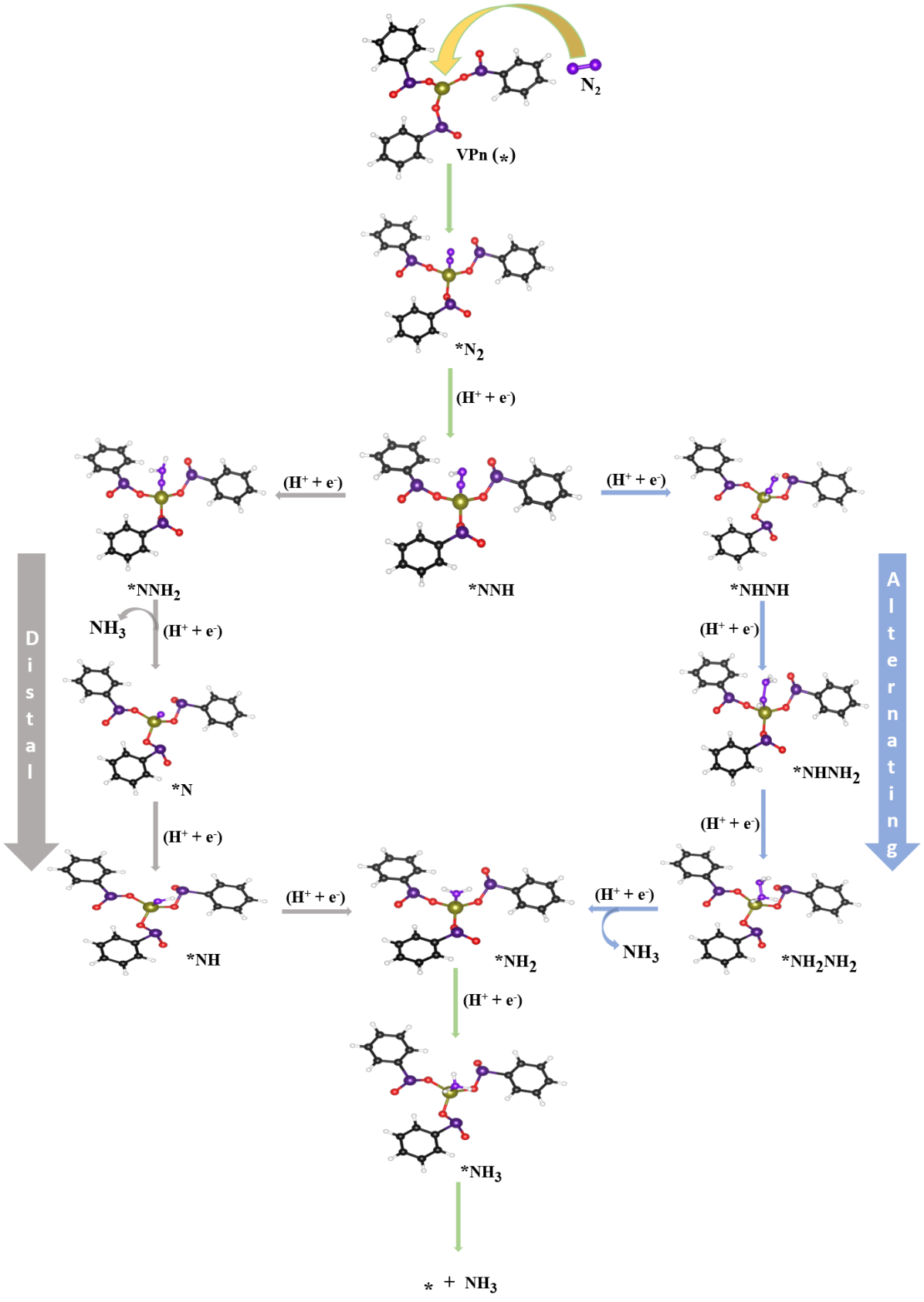

Figure S29. Schematic diagram showing the two possible pathways (associative alternating and associative distal) involving all the DFT optimized structures for the electrochemical NRR over VPn catalyst.

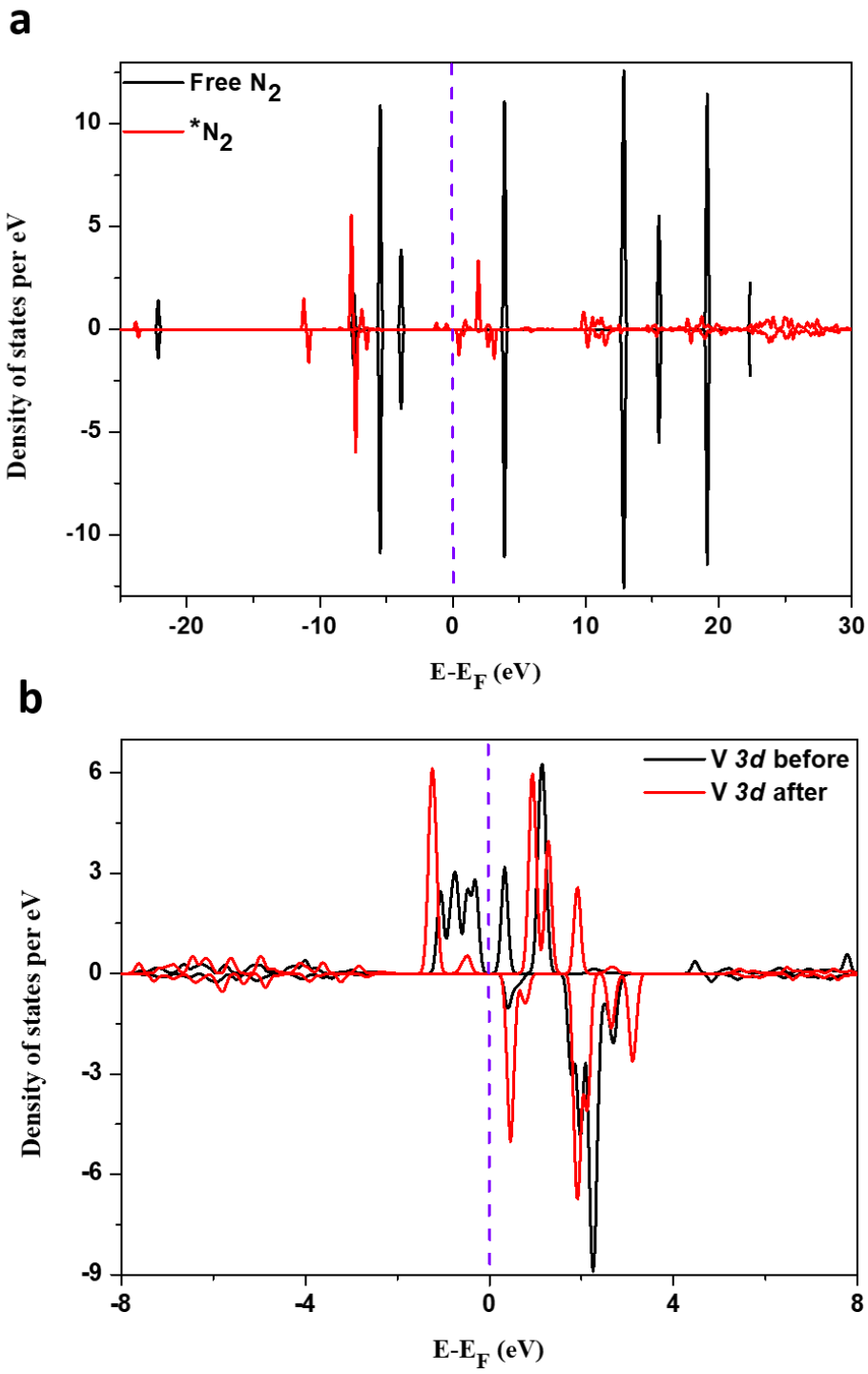

Figure S30. Projected density of states (PDOS) of (a) N_2 and (b) V 3d orbitals before and after N_2 adsorption near the Fermi level. The Fermi level is set to zero.

Importance and performance of the vanadium phosphonate with respect to the vanadium oxides, phosphides, and sulfides:

Vanadium-based complexes,[14] oxides,[15-21] phosphides,[22,23] sulfides,[24-27] carbides,[28,29,] and nitrides[30] are also active in the electrocatalysis of the NRR. The current efficiency for these catalysts is, however, of lower value. For example, transition-metal oxides (TMOs) were typically recognized as NRR active materials due to their improper hydrogen adsorption energy. Meanwhile, the poor conductivity and electron-rich surface of TMOs hinder N_2 adsorption and enhance energy consumption. Hence, the NRR application of TMOs is substantially hampered by these problems.[31] Also, V_2O_3 is less poisonous amid various vanadium oxides, but its inherent low electrical conductivity is detrimental to its electrochemical performance towards NRR.[32]

Recent theoretical calculations and experimental observations indicate that transition-metal nitrides (TMNs) are viable NRR electrocatalysts under ambient atmospheres via a Mars-van Krevelen mechanism. Although TMNs have superior chemical stability and conductivity than comparable TMOs, they are also more likely to suffer HER side effects.[31] Vanadium nitride (VN) is active for electrochemical NRR. However, such nitride suffers from using NH_3 as an N source for catalyst preparation. In addition to that, the application of VN in electrochemical systems may be constrained by the leaching phenomenon inside the electrolyte solution, especially for the electrochemical ammonia synthesis by NRR, where the retention of catalytic activity and selectivity of the catalysts persist as significant challenges.[33] Also, the employment of TMNs towards NRR suffers from the use of N-containing precursors and the deactivation of surface active sites on the catalysts.[34] So, research interests have focused on developing a unique species transition-metal oxynitride (TMON) that may resolve all of the abovementioned problems by combining the beneficial attributes of both TMOs with TMNs. Xu and colleagues conducted the mechanistic investigation of NRR on vanadium nitride nanoparticles (VN NPs).

This study revealed the existence of numerous vanadium oxide, oxynitride, and nitride on the surface; among these, the vanadium oxynitride ($VN_{0.7}O_{0.45}$) turned out to be an active phase for NRR. They hypothesized that conversion from $VN_{0.7}O_{0.45}$ to VN would result in catalyst deactivation. Specifically, the surface oxygen underwent reductive leaching, followed by the adsorption and dissociation of N_2 molecules to fill the vacancy, thus creating a fully clean VN surface that was inactive towards the NRR due to the tightly bound nitrogen atoms.[35-37]

Metal phosphide's surface has several coordinated unsaturated active sites that facilitate the bonding of nitrogen-related intermediates, making it a promising option for electrochemical NRR. The transition metal phosphide's electrochemical NRR performance and Faradaic efficiency can be increased by controlling its shape and doping. However, it is insufficient to meet the current needs of industrialization. Additionally, metal phosphides cannot be used in long-term electrocatalytic processes due to their low conductivity and stability, thus limiting their practical application.[34]

Transition metal carbides and sulfides can catalyse N_2 electroreduction to ammonia at ambient temperatures. However, transition metal carbides and sulfides are extensively studied and established as electrocatalysts for hydrogen evolution. As a result, they do not appear to be suitable as electrocatalysts for N_2 reduction.[38] Consequently, it is crucial to investigate novel, highly active vanadium-based NRR electrocatalysts.

In this work, we have synthesized and explored microporous vanadium phosphonate (VPn) as an electrocatalyst toward NRR, which stands out from other vanadium-based materials primarily due to their unique collaborative properties arising from their distinctive hybrid backbone. Such a new class of hybrid metal phosphonate can be considered as nanocomposites in which the organic and inorganic counterparts are interconnected, exhibiting the superior benefits of both the inorganic and organic skeletons. Microporous vanadium phosphonate possesses a reasonable surface area and tunable pore sizes, making them excellent candidates

for adsorption applications. Their microporous nature provides a large number of active sites for catalytic reactions, leading to their catalytic activity and selectivity towards NRR, owing to their accessibility to collaborate the benefits of both porous materials and periodic organic-inorganic skeleton architectures. After long-term stability, the post-NRR FESEM and TEM image analysis suggested that VPn exhibits retention of structural features. The post-NRR XRD, Raman, and XPS analysis reveal that the as-prepared VPn material possesses reasonable structural and chemical stability towards NRR. The electrochemical NRR performance of our as-prepared VPn material is comparable to other vanadium-based electrocatalyst, listed in Table S14.

Table S14. NRR performance of other vanadium-based electrocatalysts as compared to VPn.

Material Type	**Electrocatalyst**	**Yield Rate**	**FE (%)**	**Electrolyte**	**Reference**
Vanadium oxide	mVO_x–rGO	18.84 $\mu g\ h^{-1}\ mg_{cat.}^{-1}$	16.97%	0.1 M Na_2SO_4	18
	VO_2@CN	0.31 $\mu mol\ h^{-1}\ mg_{cat.}^{-1}$	67.9%	0.1 M Na_2SO_4	20
	V_2O_4/rGO	24.75 $\mu g\ h^{-1}\cdot\ mg_{cat.}^{-1}$	79%	0.1 M Na_2SO_4	21
	V_2O_3/C	12.3 $\mu g\ h^{-1}\ mg_{cat.}^{-1}$	7.28%	0.1 M Na_2SO_4	32
	V_2O_3	47.2 $\mu g\ h^{-1}\ mg_{cat.}^{-1}$	12.5%	0.1 M Na_2SO_4	39
	$V_3O_7.H_2O$	36.42 $\mu g\ h^{-1}\cdot mg^{-1}$	14.20%	0.1 M Na_2SO_4	40
Vanadium carbide	V_8C_7/C	34.62 $\mu g\ h^{-1}\cdot\ mg_{cat.}^{-1}$	12.20%	0.1 M HCl	28
	□-VC	23.2 $\mu g\ h^{-1}\cdot\ mg_{cat.}^{-1}$	18.3%	0.1 M HCl	29
Vanadium sulfide	1-AAQ-PA-Fe-VS_2	31.6 $\mu g\ h^{-1}\cdot mg^{-1}$	23.5 %.	0.05 M Li_2SO_4	24
	VS_4-140	46.74 $\mu g\ h^{-1}\ mg_{cat.}^{-1}$	8.5%	0.1 M Na_2SO_4	25
	VS_2-350	20.29 $\mu g\ h^{-1}\ mg_{cat.}^{-1}$	3.86%	0.1 M HCl	26
	Flower-like VS_2	34.62 $\mu g\ h^{-1}\ mg_{cat.}^{-1}$	2.09%	0.1 M HCl	27
Vanadium phosphide	VP/VF	8.35×10^{-11} $mol\cdot s^{-1}\cdot cm^{-2}$	22%	0.1 M HCl	22

	CoVP@NiFeV-LDHs	1.6×10^{-6} mol h^{-1} cm^{-2}	13.8%	0.05 M H_2SO_4	23
Vanadium phosphonate	VPn	11.84 μg h^{-1} $mg_{cat.}^{-1}$ (Phenate method, at -0.6 V)	40.63% (at -0.5V)	0.1 M Na_2SO_4	**This work**
		11.2 μg h^{-1} $mg_{cat.}^{-1}$ (Indophenol blue method, at -0.6 V)	36.56% (at -0.5V)		

Table S15. Comparison table with reported NRR electrocatalyst.

Sl no.	**Material**	**yield rate (μg h^{-1} mg^{-1}_{cat})**	**FE(%)**	**Electrolyte**	**Reference**
1	1T″′ MoS_2	9.09	13.6	0.1M Na_2SO_4	41
2	defect-rich fluorographene nanosheet	9.3	4.2	0.1M Na_2SO_4	42
3	ZrO_2	9.63	12.1	0.1M Na_2SO_4	43
4	TiO_2/CeO_2	8.8	6.8	0.1M HCl	44
5	Cu SAs/TiO_2	6.26	12.88	0.5M K_2SO_4	45
6	HAT-700-A	5.86	11.40	0.1M HCl	46
7	MoO_{2+x}	3.95	22.1	0.1M KOH	47
8	Bi@C-900	4.22 ± 0.33	15.10 ± 0.43	0.1M Na_2SO_4	48
9	Iso-e $Si_{1.6}$	3.68	5.02	0.05M H_2SO_4	49
10	$Fe_2(MoO_4)_3$	7.5	1	0.1M Na_2SO_4	50
11	Fe-NPC	4.36	5.30	0.1M NaOH	51
12	Ni-NFV3	7.3	4.4	0.1M PBS	52
13	FeSC700	8.8 ± 1.3	6.1 ± 0.9	0.1M KOH	53
14	Fe-N/C-CPs	2.27	7.67	0.5M K_2SO_4	54
15	FePc/C	10.25	14.17	0.1M Na_2SO_4	55

16	3R MoS_2-700	8.8	1.90	0.1M Na_2SO_4	56
17	WS_2/WO_2	8.53	13.50	0.05M H_2SO_4	57
18	Pd–Ag–S PNSs	9.73	18.41	0.1M Na_2SO_4	58
19	Bi NSs	11.11	14.14	0.1M Na_2SO_4	59
20	Cu/AC-S	9.7	15.9	0.1M Na_2SO_4	60
21	NPC	0.97	4.2	0.1M HCl	61
22	RGO/WOCu	11.4	4.4	0.1M Na_2SO_4	62
23	Cu_2SnS_3-10	8.22	8.87	0.1M Na_2SO_4	63
24	KNC	6.67	8.10	0.1M Na_2SO_4	64
25	$[(bpy)_4Cu_4(C_{10}H_8SO_3)_4(OH)_4]$ $\bullet 4H_2O$	2.18	0.97	0.1M Na_2SO_4	65
26	Li-TiO2(B)	8.7	18.2	0.5M $LiClO_4$	66
27	$La_{0.5}Sr_{0.5}FeO_{3-\delta}$ ceramic oxide	11.51	0.54	0.1M Na_2SO_4	67
28	$RuAu_3$/0.3Zr-C_3N_4	5.28	11.54	0.1M KOH	68
29	etched-PdZn/NHCP	5.28	16.9	0.1M PBS	69
30	$TiO_2(V_o)$_800	3	6.5	0.1M HCl	70
31	NSG	7.7	5.8	0.1M HCl	71
32	**VPn**	**11.84** (Phenate method) (at -0.6 V)	**40.63** (at -0.5 V)	**0.1M Na_2SO_4**	**This Work**
		11.2 (Indophenol blue method) (at -0.6 V)	**36.56** (at -0.5 V)		

References:

1 H. L. Du, M. Chatti, R. Y. Hodgetts, P. V. Cherepanov, C. K. Nguyen, K. Matuszek, D. R. MacFarlane and A. N. Simonov, *Nature*, 2022, **609**, 722–727.
2 E. García-Robledo, A. Corzo and S. Papaspyrou, *Mar. Chem.*, 2014, **162**, 30–36.
3 B. H. R. Suryanto, K. Matuszek, J. Choi, R. Y. Hodgetts, H. L. Du, J. M. Bakker, C. S. M. Kang, P. V. Cherepanov, A. N. Simonov and D. R. MacFarlane, *Science (80-.).*, 2021, **372**, 1187–1191.
4 S. Smidstrup, T. Markussen, P. Vancraeyveld, J. Wellendorff, J. Schneider, T. Gunst, B. Verstichel, D. Stradi, P. A. Khomyakov, U. G. Vej-Hansen, M.-E. Lee, S. T. Chill, F. Rasmussen, G. Penazzi, F. Corsetti, A. Ojanperä, K. Jensen, M. L. N. Palsgaard, U. Martinez, A. Blom, M. Brandbyge and K. Stokbro, *J. Phys. Condens. Matter*, 2020, **32**, 015901.
5 J. P. Perdew, K. Burke and M. Ernzerhof, *Phys. Rev. Lett.*, 1996, **77**, 3865–3868.
6 S. Grimme, *J. Comput. Chem.*, 2006, **27**, 1787–1799.
7 H. J. Monkhorst and J. D. Pack, *Phys. Rev. B*, 1976, **13**, 5188–5192.
8 A. A. Peterson, F. Abild-Pedersen, F. Studt, J. Rossmeisl and J. K. Nørskov, *Energy Environ. Sci.*, 2010, **3**, 1311.
9 A. Altomare, N. Corriero, C. Cuocci, A. Falcicchio, A. Moliterni and R. Rizzi, *Cryst. Res. Technol.*, 2015, **50**, 737–742.
10 G. Lin, Q. Ju, X. Guo, W. Zhao, S. Adimi, J. Ye, Q. Bi, J. Wang, M. Yang and F. Huang, *Adv. Mater.*, , DOI:10.1002/adma.202007509.
11 R. I. Mohanty, S. Dash, A. Mukherjee, B. K. Jena, P. Bhanja and S. Basu, *Int. J. Hydrogen Energy*, 2024, **52**, 1550–1559.
12 H. Zhang, X. Xiao, X. Lu, G. Chai, Y. Sun, Y. Zhan and G. Xu, *J. Alloys Compd.*, 2015, **636**, 106–112.
13 E. Podstawka, A. Kudelski, P. Kafarski and L. M. Proniewicz, *Surf. Sci.*, 2007, **601**, 4586–4597.
14 P. Bhattacharya, D. E. Prokopchuk and M. T. Mock, *Coord. Chem. Rev.*, 2017, **334**, 67–83.
15 Y. Abghoui, A. L. Garden, J. G. Howalt, T. Vegge and E. Skúlason, *ACS Catal.*, 2016, **6**, 635–646.
16 Y. Sun, I. Sinev, W. Ju, A. Bergmann, S. Dresp, S. Kühl, C. Spöri, H. Schmies, H. Wang, D. Bernsmeier, B. Paul, R. Schmack, R. Kraehnert, B. Roldan Cuenya and P. Strasser, *ACS Catal.*, 2018, **8**, 2844–2856.
17 H. Ying, J. Bi, H. Xu, G. Wu, X. Wu, J. Hao and Z. Li, *ACS Sustain. Chem. Eng.*, 2022, **10**, 6766–6774.
18 W. Fang, J. Zhao, T. Wu, Y. Huang, L. Yang, C. Liu, Q. Zhang, K. Huang and Q. Yan, *J. Mater. Chem. A*, 2020, **8**, 5913–5918.
19 Y. Liu, X. Zhu, Q. Zhang, T. Tang, Y. Zhang, L. Gu, Y. Li, J. Bao, Z. Dai and J.-S. Hu, *J. Mater. Chem. A*, 2020, **8**, 8920–8926.
20 A. Chhetri, A. Biswas, S. Podder, R. S. Dey and J. Mitra, *Nanoscale*, , DOI:10.1039/D4NR00640B.
21 S. Chen, Y. Liang, M. Bu, Z. Dai and J. Shi, *Catal. Letters*, 2024, **154**, 1795–1805.
22 P. Wei, Q. Geng, A. I. Channa, X. Tong, Y. Luo, S. Lu, G. Chen, S. Gao, Z. Wang and X. Sun, *Nano Res.*, 2020, **13**, 2967–2972.
23 M. Arif, G. Yasin, L. Luo, W. Ye, M. A. Mushtaq, X. Fang, X. Xiang, S. Ji and D. Yan, *Appl. Catal. B Environ.*, 2020, **265**, 118559.
24 Z. Xiu, M. Zheng, J. Li, F. Wei, C. Dong, M. Zhang, X. Zhou and X. Han, *ChemSusChem*, , DOI:10.1002/cssc.202200741.

25 L. Yang, S. Wang, C. Qian and S. Zhou, *ACS Appl. Energy Mater.*, 2023, **6**, 8830–8837.
26 L. Zhao, Y. Xiong, X. Wang, R. Zhao, X. Chi, Y. Zhou, H. Wang, Z. Yang and Y. Yan, *Small*, , DOI:10.1002/smll.202106939.
27 L. Zhao, R. Zhao, Y. Zhou, X. Wang, X. Chi, Y. Xiong, C. Li, Y. Zhao, H. Wang, Z. Yang and Y.-M. Yan, *J. Mater. Chem. A*, 2021, **9**, 24985–24992.
28 J. Feng, X. Zhu, Q. Chen, W. Xiong, X. Chen, Y. Luo, A. A. Alshehri, K. A. Alzahrani, Z. Jiang and W. Li, *J. Mater. Chem. A*, 2019, **7**, 26227–26230.
29 C. Zhang, D. Wang, Y. Wan, R. Lv, S. Li, B. Li, X. Zou and S. Yang, *Mater. Today*, 2020, **40**, 18–25.
30 X. Yang, S. Kattel, J. Nash, X. Chang, J. H. Lee, Y. Yan, J. G. Chen and B. Xu, *Angew. Chemie Int. Ed.*, 2019, **58**, 13768–13772.
31 B. Chang, L. Deng, S. Wang, D. Shi, Z. Ai, H. Jiang, Y. Shao, L. Zhang, J. Shen, Y. Wu and X. Hao, *J. Mater. Chem. A*, 2020, **8**, 91–96.
32 R. Zhang, J. Han, B. Zheng, X. Shi, A. M. Asiri and X. Sun, *Inorg. Chem. Front.*, 2019, **6**, 391–395.
33 R. Manjunatha, A. Karajić, H. Teller, K. Nicoara and A. Schechter, *ChemCatChem*, 2020, **12**, 438–443.
34 J. Li, F. Wei, C. Dong, Z. Wang, Z. Xiu and X. Han, *Mater. Today Energy*, 2021, **21**, 100766.
35 X. Yang, J. Nash, J. Anibal, M. Dunwell, S. Kattel, E. Stavitski, K. Attenkofer, J. G. Chen, Y. Yan and B. Xu, *J. Am. Chem. Soc.*, 2018, **140**, 13387–13391.
36 W. Guo, K. Zhang, Z. Liang, R. Zou and Q. Xu, *Chem. Soc. Rev.*, 2019, **48**, 5658–5716.
37 S. B. Patil and D. Wang, *Small*, , DOI:10.1002/smll.202002885.
38 G. Qing, R. Ghazfar, S. T. Jackowski, F. Habibzadeh, M. M. Ashtiani, C.-P. Chen, M. R. Smith and T. W. Hamann, *Chem. Rev.*, 2020, **120**, 5437–5516.
39 N. Wang, Q.-S. Song, W.-J. Liu and J. Zhang, *Front. Energy Res.*, , DOI:10.3389/fenrg.2020.602438.
40 Y. Sun, S. Ding, C. Zhang, J. Duan and S. Chen, *J. Mater. Chem. A*, 2021, **9**, 1603–1609.
41 G. Lin, Q. Ju, X. Guo, W. Zhao, S. Adimi, J. Ye, Q. Bi, J. Wang, M. Yang and F. Huang, *Adv. Mater.*, 2021, **33**, 2007509.
42 J. Zhao, J. Yang, L. Ji, H. Wang, H. Chen, Z. Niu, Q. Liu, T. Li, G. Cui and X. Sun, *Chem. Commun.*, 2019, **55**, 4266–4269.
43 J. Xia, H. Guo, M. Cheng, C. Chen, M. Wang, Y. Xiang, T. Li and E. Traversa, *J. Mater. Chem. A*, 2021, **9**, 2145–2151.
44 B. Yan, S. Hu, C. Bu, Y. Peng, H. Han, X. Xu, Y. Liu, J. Yu and Y. Dai, *ChemCatChem*, , DOI:10.1002/cctc.202300076.
45 Z. Zhao, K. Li, J. Liu, J. Mao and Y. Lin, *Small*, , DOI:10.1002/smll.202206626.
46 W. Zhang, S. Zhan, Q. Qin, T. Heil, X. Liu, J. Hwang, T. H. Ferber, J. P. Hofmann and M. Oschatz, *Small*, , DOI:10.1002/smll.202204116.
47 J. Wang, Z. Jiang, G. Peng, E. Hoenig, G. Yan, M. Wang, Y. Liu, X. Du and C. Liu, *Adv. Sci.*, 2022, **9**, 1–8.
48 Y. Wan, H. Zhou, M. Zheng, Z. Huang, F. Kang, J. Li and R. Lv, *Adv. Funct. Mater.*, , DOI:10.1002/adfm.202100300.
49 G. Y. Zhai, D. Xu, S. N. Zhang, Z. H. Xue, H. Su, Q. Y. Yu, H. H. Wang, X. Lin, Y. X. Lin, L. H. Sun, X. H. Li and J. S. Chen, *Adv. Funct. Mater.*, 2020, **30**, 1–7.
50 C. Chen, Y. Liu and Y. Yao, *Eur. J. Inorg. Chem.*, 2020, **2020**, 3236–3241.
51 P. Song, H. Wang, X. Cao, N. Liu, Q. Wang and R. Wang, *ChemElectroChem*, 2020, **7**, 212–216.
52 F. Bai, X. Qu, C. Li, S. Liu, J. Sun, X. Chen and W. Yang, *ACS Appl. Mater. Interfaces*, 2022, **14**, 28033–28043.

53 M. I. Ahmed, L. J. Arachchige, Z. Su, D. B. Hibbert, C. Sun and C. Zhao, *ACS Catal.*, 2022, **12**, 1443–1451.
54 Y. Liu, Z. Zhao, W. Wei, X. Jin, G. Wang, K. Li and Y. Lin, *ACS Appl. Nano Mater.*, 2021, **4**, 13001–13009.
55 C. He, Z. Y. Wu, L. Zhao, M. Ming, Y. Zhang, Y. Yi and J. S. Hu, *ACS Catal.*, 2019, **9**, 7311–7317.
56 B. Fang, J. Yao, X. Zhang, L. Ma, Y. Ye, J. Tang, G. Zou, J. Zhang, L. Jiang and Y. Sun, *New J. Chem.*, 2021, **45**, 2488–2495.
57 Y. Ling, F. M. D. Kazim, S. Ma, Q. Zhang, K. Qu, Y. Wang, S. Xiao, W. Cai and Z. Yang, *J. Mater. Chem. A*, 2020, **8**, 12996–13003.
58 H. Wang, S. Liu, H. Zhang, S. Yin, Y. Xu, X. Li, Z. Wang and L. Wang, *Nanoscale*, 2020, **12**, 13507–13512.
59 Y. Xu, T. Ren, S. Yu, H. Yu, S. Yin, Z. Wang, X. Li, L. Wang and H. Wang, *Sustain. Energy Fuels*, 2020, **4**, 3334–3339.
60 S. Zhang, W. Li, Y. Liu, J. Wang, G. Wang, Y. Zhang, M. Han and H. Zhang, *Inorg. Chem. Front.*, 2019, **6**, 2832–2836.
61 P. Song, H. Wang, L. Kang, B. Ran, H. Song and R. Wang, *Chem. Commun.*, 2019, **55**, 687–690.
62 L. Hu, K. Liu, Y. Guo, J. Feng, X. Ding, W. Li, X. Su, M. Gao, Z. Li, H. Zhang, Y. Ren and T. Wei, *J. Colloid Interface Sci.*, 2023, **644**, 285–294.
63 X. He, Z. Ling, X. Peng, X. Yang, L. Ma and S. Lu, *Electrochem. commun.*, 2023, **148**, 107441.
64 L. Zhang, H. Shoushuang, J. Bao, L. Liu, T. Ye, X. Cong, K. Uvdal and Z. Hu, *J. Alloys Compd.*, 2022, **910**, 164759.
65 W. Wang, J. Z. Li, S. J. Luo, Z. X. Yao and K. G. Liu, *Inorganica Chim. Acta*, 2022, **534**, 120809.
66 R. Zhao, G. Wang, Y. Mao, X. Bao, Z. Wang, P. Wang, Y. Liu, Z. Zheng, Y. Dai, H. Cheng and B. Huang, *Chem. Eng. J.*, 2022, **430**, 133085.
67 Y. Xu, X. Xu, N. Cao, X. Wang, X. Liu, M. Fronzi and L. Bi, *Int. J. Hydrogen Energy*, 2021, **46**, 10293–10302.
68 W. Lin, S. Yao, H. Chen, S. Li, Y. Xia, Y. Yao, J. Li, D. Cheng and J. Fu, *J. Energy Chem.*, 2020, **53**, 109–115.
69 M. Ma, X. Han, H. Li, X. Zhang, Z. Zheng, L. Zhou, J. Zheng, Z. Xie, Q. Kuang and L. Zheng, *Appl. Catal. B Environ.*, 2020, **265**, 118568.
70 Z. Han, C. Choi, S. Hong, T. S. Wu, Y. L. Soo, Y. Jung, J. Qiu and Z. Sun, *Appl. Catal. B Environ.*, , DOI:10.1016/j.apcatb.2019.117896.
71 Y. Tian, D. Xu, K. Chu, Z. Wei and W. Liu, *J. Mater. Sci.*, 2019, **54**, 9088–9097.